# Advanced Image Reconstruction and Sampling Pattern Optimization in Silent MRI

by

Haowei Xiang

A dissertation submitted in partial fulfillment
of the requirements for the degree of
Doctor of Philosophy
(Electrical and Computer Engineering)
in the University of Michigan
2024

Doctoral Committee:

Professor Jeffrey A. Fessler, Co-Chair
Professor Douglas C. Noll, Co-Chair
Professor Thomas Chenevert
Assistant Professor Yun Jiang
Associate Professor Zhongming Liu

Haowei Xiang

haoweix@umich.edu

ORCID iD: 0000-0001-7598-9480

# TABLE OF CONTENTS

**Chapter**

# LIST OF FIGURES

# LIST OF ACRONYMS

**MRI** magnetic resonance imaging

**FMRI** functional magnetic resonance imaging

**RF** radiofrequency

**ZTE** zero echo-time

**PD** proton density

**FID** free induction decay

**GRE** gradient echo

**MBIR** model-based image reconstruction

**BOLD** blood-oxygen level dependent

**QSM** quantitative susceptibility mapping

**UNFOLD** Unaliasing by Fourier-encoding the overlaps in the temporal dimension

**LLR** locally low-rank

**FFT** fast (discrete) Fourier transform

**NUFFT** non-uniform fast (discrete) Fourier transform

**DCT** discrete cosine transform

**DFT** discrete Fourier transform

**CS** compress sensing

**MAP** maximum a posteriori

**SVD** singular value decomposition

**PCA** principle component analysis

**AWGN** additive white Gaussian noise

**CNN** convolutional neural network

**TV** Total Variation

**PSNR** peak signal-to-noise ratio

**NRMSE** normalized root mean square error

**NRMSD** normalized root mean square difference

**SNR** signal-to-noise ratio

**ADMM** alternating direction method of multipliers

# LIST OF SYMBOLS

| | |
|---|---|
| $\boldsymbol{x}$ | a signal or image |
| $\hat{\boldsymbol{x}}$ | an image estimate |
| $\boldsymbol{x}^*$ | a minimizer of a function |
| $\boldsymbol{y}$ | measurements |
| $\boldsymbol{A}$ | the measurement/system/forward model |
| $\boldsymbol{e}_i$ | $i$th standard basis vector |
| $\|\cdot\|_p$ | a vector p-norm |
| $\vert\vert\vert\cdot\vert\vert\vert_p$ | an operator or matrix norm |
| $\nabla\cdot$ | the gradient operator |
| $\mathsf{R}(\cdot)$ | a regularization function |
| $\boldsymbol{A}'$ | Hermitian transpose of $\boldsymbol{A}$ |
| $\boldsymbol{A}^T$ | Transpose of $\boldsymbol{A}$ |
| $\mathcal{R}(\cdot)$ | the range space/set of a function |
| $\mathcal{N}(\cdot)$ | the null space/set of a function |
| $\operatorname{prox}_f(\boldsymbol{v})$ | proximal operator: $\arg\min_{\boldsymbol{x}} \frac{1}{2}\|\boldsymbol{v}-\boldsymbol{x}\|_2^2 + f(\boldsymbol{x})$ |
| $\mathcal{P}_C(\boldsymbol{v})$ | projection onto set $C$: $\arg\min_{\boldsymbol{x}\in C} \frac{1}{2}\|\boldsymbol{v}-\boldsymbol{x}\|_2^2$ |

# ABSTRACT

Silent magnetic resonance imaging (MRI) is a technology that allows for MRI scans to be conducted with less acoustic noise than traditional MRI technologies. This technology is important for a few reasons: First, the loud noises generated by traditional MRI machines can be uncomfortable for some patients, particularly those with anxiety disorders, dementia, or sensory sensitivities. Second, silent MRI can be useful in auditory and speaking studies. Third, the noise generated by traditional MRI machines can interfere with speech communication, making it difficult for healthcare providers to communicate with patients during the scan.

Model-based image reconstruction (MBIR) is a technique in MRI that uses mathematical models and MRI physics to suppress image noise, reduce acquisition time, and improve image quality, especially in dynamic and quantitative MRI. In this study, we first combined the silent MRI and MBIR and developed reconstruction method for both static and dynamic MRI to reduce image noise and artifacts, improve image quality and resolution, and boost functional/quantitative analysis. Secondly, we optimized sampling trajectory to improve the k-space coverage and reduce image artifacts in the reconstruction. Lastly, we proposed methods of designing shaped RF pulse, and developed variable flip angle schemes to create more uniform longitudinal magnitization.

Through model-based image reconstruction, we found that signal modeling using two-system matrices resulted in reduced signal artifact from overlapping echoes and improved SNR of close to 1.4 relative to reconstruction with a single system matrix. The development of joint reconstruction methods, which estimate multiple echoes simultaneously, played a crucial role in improving the temporal signal-to-noise ratio and reducing noise artifacts. The k-space trajectory optimization can improve image quality and reduce undersampling artifact by sampling more efficiently. Additionally, the optimization of RF pulse designs facilitated better magnetization and more uniform signal excitation across the imaging volume, maximizing total magnetization and achieving more uniform excitation profiles. These findings suggest that by carefully designing reconstruction algorithms, sampling patterns, and excitation modules, the image quality of silent MRI can be improved for broader use in both research and clinical settings.

# CHAPTER 1

# Introduction

Magnetic resonance imaging (MRI) has become the primary tool for noninvasive imaging of human brain activity. Nevertheless, the loud acoustic noise produced during MRI procedures remains a significant issue. For instance, this noise can lead to discomfort and anxiety in patients [1], particularly affecting vulnerable groups such as children and patients with dementia. Additionally, acoustic noise serves as an extraneous sensory stimulus [2, 3, 4], which can alter the blood-oxygen level dependent (BOLD) response based on its loudness [5] and duration [6]. There are multiple ways [7] in which acoustic noise can interfere with functional MRI (FMRI) tasks and degrade the quality of measured signals. First, noise from the scanner activates the auditory pathway (including the auditory cortex), thereby reducing sensitivity to experimental stimuli [8]. Second, stimuli may require additional cognitive processes [9] (such as verbal working memory or performance monitoring). Lastly, scanner noise can cause participant discomfort and increase attentional demands, even in non-auditory tasks.

Various sources contribute to acoustic noise, including gradient coils, radio-frequency (RF) components, cryogenic pumps, and air circulating systems. However, the primary source of acoustic noise is the Lorentz forces resulting from rapidly changing currents in the magnetic field gradient coils, which are essential for spatial localization [10]. Reducing the acoustic noise level can be achieved through hardware modifications like gradient designs and shielding [11], implementing quiet scanning modes provided by vendors [12], and developing specific pulse sequence designs. Some MRI vendors offer a suite of "silent" MRI pulse sequences. These methods aim to minimize acoustic noise in structural imaging, either by slowing down gradient changes—reducing noise at the expense of acquisition time, or by employing special pulse sequences designed to be quieter (e.g., RUFIS[13], zTE[14], PETRA[15]).

The looping star pulse sequence [16] is among the silent MRI methods utilized for quantitative susceptibility mapping (QSM), T2* weighted imaging, and FMRI [17]. This sequence employs multiple RF pulses and slowly varying gradients, substantially reducing acoustic noise compared to the standard echo planar imaging (EPI) method. This characteristic makes it ideal for scenarios requiring low acoustic noise, such as pediatric MRI [18] and auditory functional MRI tasks [19]. The looping star technique is a true 3D acquisition with frequent sampling at low k-space frequencies, enabling rapid sampling of physiological noise and quick head motion estimation. Additionally, it may be resistant to intra-object motion due to the central k-space oversampling. However, the use of multiple RF pulses with slowly varying gradients complicates k-space trajectories, making the reconstruction process more challenging. The most significant artifact issue is the overlapping-echo effect, that occurs when signals from multiple excitation pulses are present simultaneously while traversing k-space locations.

Several methods have been proposed to mitigate overlapping echo artifacts. The first method [16] assumes that the echo-out and echo-in signals dominate the acquired signal at the beginning and end of the sampling period, thereby separating the overlapping echoes at the cost of lower SNR and spatial resolution. The second method, RF-phase cycling, involves an additional scan with a $\pi$ RF phase change, separating overlapping echoes by performing a linear combination of signals from both scans. This method can increase SNR by $\sqrt{2}$ but at the expense of doubled scan time. The third method, coherence-resolved looping-star [20], uses half as many RF pulses with increased time intervals to separate the echoes. This approach can be considered a standard windowing method [17] but starts with fewer spokes and a higher resolution input. This method requires longer scan times for structural MRI and has worse temporal resolution in fMRI tasks when matching the overall undersampling factor. None of the existing methods can separate overlapping echoes without compromising scan time, spatial resolution, or SNR.

In this work, we aim to enhance the looping-star method by addressing the critical need for improved spatial and temporal resolution, signal-to-noise ratio, and robustness to physiological noise and other image artifacts through innovative image acquisition and reconstruction techniques. For example, a model-based reconstruction approach [21] can theoretically resolve overlapping echoes and maintain resolution without increasing scan time. Optimizing k-space trajectories can significantly improve sampling efficiency and reduce image artifacts. Spatial-temporal reconstruction using UNFOLD and locally low-rank techniques can produce steady time courses, improved activation maps, and gains in temporal SNR in fMRI.

Model-based image reconstruction (MBIR) encompasses a family of non-linear reconstruction methods that have proven to be flexible for various inverse problems and capable of producing high-quality estimates. It employs mathematical models to suppress image noise, reduce acquisition time, and enhance image quality, particularly in dynamic and quantitative MRI. The significance of MBIR in MRI lies in its capacity to overcome some limitations of traditional MRI techniques. One primary advantage of MBIR is its ability to reduce undersampling artifacts and improve image quality. By utilizing mathematical models to fill in missing data and reduce image noise, MBIR results in higher resolution, more efficient sampling, and superior image quality. This capability is particularly beneficial for 3D silent MRI pulse sequences due to their low SNR and high acceleration factors. Additionally, MBIR can enhance dynamic and quantitative MRI by better separating signals from the background image and yielding improved results.

The organization of this thesis proposal is as follows. Ch. 2 provides background. Ch. 3 describes our recent publication [22] that introduces the model-based method to address the overlapping echoes problems and improve the image quality and resolutions in looping star MRI. Ch. 4 describes a spatial-temporal reconstruction method that combines MBIR, UNFOLD, and LLR to improve the spatial and temporal resolution. Ch. 5 describes a parameterization for looping-star gradient waveforms and a learning-based approach to optimize the gradient and k-space trajectories. Ch. 6 describes a few works in progress: joint reconstruction of the FID and GRE signals for better quantitative map estimation and optimization of the RF excitation for silent ZTE MRI Ch. 7 describes the potential future directions.

# CHAPTER 2

# Background

This thesis focuses on designing novel silent pulse sequences, developing model-based reconstruction methods for dynamic MRI and quantitative analysis, and optimizing sampling trajectories and flip angles to resolve potential overlapped echoes, improve image quality, and reduce image artifact. in MRI. This chapter reviews the origin of acoustic noise, the mathematics of inverse problems, and the generic framework for addressing the artifacts. We present MRI in sufficient detail for this work where inverse problems arise. Having presented concrete inverse problems, we describe the overlapping echoes problem, and its solution which we will use in several chapters.

## 2.1 Image Reconstruction

### 2.1.1 Inverse Problems

In signal processing and imaging, it is common to collect samples of a signal of interest indirectly, by measuring some function of the signal. For example, in imaging, the measurements may be obtained by subsampling the original signal, or by measuring a projection or transform of the signal. In the linear case, we can describe how the measurements $\boldsymbol{y}$ are obtained from the true signal $\boldsymbol{x}_{\text{true}}$ using the linear measurement model:

$$\boldsymbol{y} = \boldsymbol{A}\boldsymbol{x}_{\text{true}} + \boldsymbol{\epsilon}, \tag{2.1}$$

where $\boldsymbol{A}$ represents the linear measurement operator or matrix that maps the true signal to the measured signal, and $\boldsymbol{\epsilon}$ is an additive noise term, often modeled as additive complex white Gaussian noise in MRI.

The measurement operator $\boldsymbol{A}$ can be thought of as a mapping from the space of possible signals to the space of possible measurements. However, because the measurements are generally obtained through a process that removes information from the original signal (such as through blurring or undersampling), the measurement operator is typically a wide matrix, meaning that there are more unknowns than measurements in the signal. In such cases, estimating the true signal $\boldsymbol{x}_{\text{true}}$ from the measurements $\boldsymbol{y}$ and the measurement operator $\boldsymbol{A}$ is an underdetermined inverse problem, as there are many possible signals $\boldsymbol{x}$ that could give rise to the same measurements $\boldsymbol{y}$. Various paradigms have been developed to tackle this problem, including classical linear or filtering-based methods such as filtered back projection for CT or Wiener filtering for deconvolution problems. While these methods are fast and efficient, their results are often of insufficient quality for practical use.

MBIR is a family of reconstruction methods that has shown to be both flexible to a variety of inverse problems and able to produce high-quality estimates. MBIR typically involves solving an optimization problem that incorporates a prior model of the true signal, which may be learned from data or specified based on prior knowledge about the signal. Various algorithms, such as iterative methods or convex optimization techniques, can then be used to find the optimal solution to the optimization problem.

In this work, MBIR is the main framework used for image reconstruction, as it has shown to be a powerful and versatile approach for solving underdetermined inverse problems in imaging.

### 2.1.2 Model-Based Image Reconstruction

MBIR has its foundations in Bayesian MAP (Maximum A Posteriori) estimation. MAP estimation aims to maximize the probability of our estimate given our measurements, which is represented by the posterior distribution $\mathsf{p}(\boldsymbol{x}|\boldsymbol{y})$. This posterior distribution, derived from Bayes' theorem, combines prior knowledge about the signal and the likelihood of observing the measured data given that signal. Bayes' Rule is used to rewrite the posterior as shown in Equation (2.2).

$$\mathsf{p}(\boldsymbol{x}|\boldsymbol{y}) = \frac{\mathsf{p}(\boldsymbol{y}|\boldsymbol{x})\,\mathsf{p}(\boldsymbol{x})}{\mathsf{p}(\boldsymbol{y})}. \tag{2.2}$$

To maximize the left-hand side, we can equivalently maximize the right-hand side. When maximizing with respect to $\boldsymbol{x}$, we can drop $\mathsf{p}(\boldsymbol{y})$ as it serves as a constant scaling factor. Applying $-\log(\cdot)$ to write the problem as

$$\hat{\boldsymbol{x}} = \arg\min_{\boldsymbol{x}} -\log(\mathsf{p}(\boldsymbol{y}|\boldsymbol{x})) - \log(\mathsf{p}(\boldsymbol{x}))\,. \tag{2.3}$$

yields the MAP estimation problem, as expressed in Equation (2.3).

In the context of MAP estimation, the first term is often called the negative log-likelihood, which encodes the measurement dependence of our estimate. For instance, in the case of additive white Gaussian noise (AWGN) and the measurement model (2.1), the negative log-likelihood is proportional to $\|\boldsymbol{A}\boldsymbol{x} - \boldsymbol{y}\|_2^2$. The second term, known as the negative log-prior or simply the prior, encodes our preconceived assumptions about which signals $\boldsymbol{x}$ are more probable, irrespective of measurements. Therefore, MAP provides a modular estimation framework that models both measurement dependence and signal characteristics. However, it is challenging to encode common signal characteristics as a prior probability distribution.

MBIR departs from the probabilistic interpretation of Equation (2.3). To distinguish it from MAP interpretation, the first term is referred to as the *data-fidelity* term instead of the negative log-likelihood, while the second term is called *regularization* instead of a prior. However, it is worth noting that these MAP terms are still used informally in the context of MBIR, despite the lack of statistical interpretability of many regularization functions.

Therefore, in MBIR, a common estimation problem for Equation (2.1) can be formulated as minimizing the sum of the data-fidelity term and a regularization term. The regularization term penalizes deviation from our signal model, while the hyperparameter controls the trade-off between data-fit and regularization. However, developing effective signal and image models along with corresponding regularization functions can be challenging. The ideal image model should be broad enough to describe all plausible true images while being discriminating enough to reject noise and artifacts. Thus, developing an effective regularization function is a central goal in the context of MBIR.

## 2.2 Magnetic Resonance Imaging

In MRI, a strong main magnetic field is applied to align the magnetic moments of hydrogen atoms in the body. RF pulses are then applied to perturb these aligned moments, causing them to precess. When the RF pulse is turned off, the precessing moments emit a signal, which is detected by a coil surrounding the body. This signal is used to reconstruct an image of the body's internal structure.

Multi-coil imaging in MRI refers to the use of multiple coils to detect the emitted signal. Each coil has a different spatial sensitivity map and detects a somewhat different signal, which can be combined to obtain a higher quality image. In MRI, measurements are collected sequentially in k-space, the spatial Fourier space of the true image. When k-space is fully sampled, the image can be reconstructed using an inverse DFT. However, to accelerate scan times, k-space is often undersampled.

Undersampling k-space can result in spatial aliasing artifacts in the reconstructed image. To overcome this, various methods have been developed, including compressed sensing, parallel imaging, and partial Fourier techniques. These methods exploit the fact that the information content of the signal is not evenly distributed in k-space, allowing for faster acquisition times while still producing high-quality images.

In summary, while a full exposition of the physics of MRI is not necessary for the purposes of this work, an understanding of multi-coil imaging and the challenges of undersampling k-space is important for obtaining high-quality images in a timely manner.

### 2.2.1 MRI physics and signal model

The system model $\boldsymbol{A} = \boldsymbol{U}\boldsymbol{F}$ in the context of MRI represents the process of acquiring image data by performing Fourier measurements and then subsampling the Fourier coefficients. The undersampling operator $\boldsymbol{U}$ reduces the number of Fourier coefficients that are acquired, resulting in a lower-dimensional measurement vector. This undersampling is often used in MRI to reduce acquisition time and improve patient comfort.

### 2.2.2 Acoustic Noise in MRI

There are multiple sources of acoustic noise during an MRI scan. The primary source of acoustic noise in MRI machines is the rapid switching of magnetic gradients. MRI machines use powerful magnets and magnetic gradients to create images of the body's tissues. The gradients are necessary to create detailed images, but they produce rapid changes in the magnetic field, resulting in a loud knocking or thumping noise. The acoustic noise produced by MRI machines can range from 80 to 130 decibels, which can be uncomfortable or even painful for patients. In addition to the gradients, other components of the MRI machine can also contribute to the overall acoustic noise level. For example, cooling systems used to keep the MRI machine cool can also generate a constant whirring and thumping noise.

## 2.3 Silent Zero Echo-Time MRI

In MRI, echo time refers to the time interval between the application of the RF excitation pulse and the peak of the signal or echo detected by the receiver coil. Zero Echo Time (ZTE) MRI is a technique that allows for imaging of tissues that are not easily visualized using traditional MRI techniques. The technique uses RF excitation to create images with very short echo times, which is important for imaging tissues that have very short T2 relaxation times, such as bone or lung tissue.

This section provides an overview of the mechanics of the ZTE pulse sequence in MRI, focusing on the RF excitation and k-space encoding processes. Additionally, it highlights common image artifacts associated with ZTE imaging and describes the acoustic noise behavior of this technique.

### 2.3.1 RF Excitation in the Presence of Gradient

As illustrated in Figure 2.1 [23], ZTE imaging involves RF excitation in the presence of the readout gradients, which presents two unique challenges. Firstly, while the requirement for the RF pulse to encompass the full receive imaging bandwidth is common across many imaging sequences, in ZTE imaging it is particularly critical. This ensures uniform excitation regardless of the readout direction [24], meaning the RF pulse must cover a broad range of frequencies to uniformly excite all regions of interest, which can be especially challenging in ZTE due to its continuous readout nature. Secondly, the finite time it takes to switch from RF transmit to receive mode, known as the dead-time gap, leads to missed samples at the beginning of the readout [25]. This gap can cause artifacts such as banding or blurring in the final image due to the loss of initial data points, which are crucial for accurate image reconstruction. The dead-time gap can be minimized by using fast-switching RF coils and optimized pulse sequences, but some degree of dead-time gap is still present in most ZTE imaging protocols. These challenges underscore the importance of carefully optimizing ZTE imaging parameters to achieve high-quality images with minimal artifacts. To address the technical challenges in ZTE imaging, it is essential to develop novel silent MRI pulse sequences and improving image quality and reconstruction methods, which are core focuses of my research.

### 2.3.2 Silent 2D and 3D k-space sampling

Sampling the free induction decay (FID) signal, which is the observable signal decay emitted by excited hydrogen nuclei returning to their equilibrium state, in the presence of a constant readout gradient naturally leads to a 3D centre-out radial k-space sampling scheme (illustrated in Fig. 2.1B). To achieve full spherical k-space coverage, the readout direction is updated in between excitations. For a cubic image matrix size of $N \times N \times N$, each spoke contains N sampling points. The number of (two-sided) spokes required to fulfil the

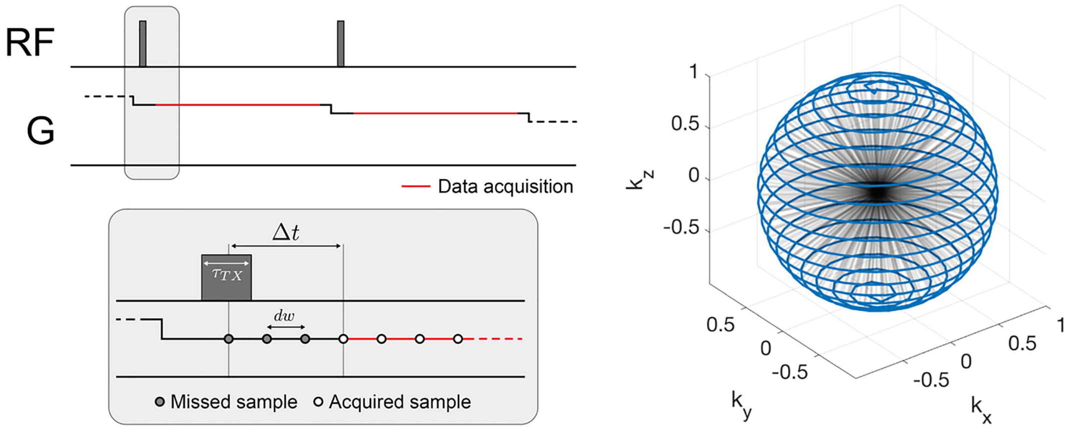

(A)

(B)

**FIG** 2.1 – (A) The simplified ZTE pulse sequence diagram with two spokes is shown above. The RF excitation and the gradient waveform are plotted on one axis. A magnified view of the RF excitation part of the spoke is also shown, indicating the dead-time gap after RF excitation. (B) The 3D view of spoke distribution in k-space is shown below. The endpoints of each spoke are connected by a blue line. (Taken from [23])

Nyquist criterion (2N) at a maximum k-space radius is determined by the surface area of the k-space sphere, which is proportional to $(N/2)^2$. For equidistant radial sampling, the density decreases inversely proportional to the squared radius. However, accelerating a 3D radial acquisition through angular undersampling, i.e., reducing the number of spokes, would reduce the SNR and produce undersampling artefacts manifesting as streaking.

The non-selective excitation in ZTE can excite spins outside the FOV, which includes plastic materials such as the RF coil and patient table. To avoid aliasing of such signals, radial oversampling is used to push the aliasing-sphere outside the imaging FOV. Radial oversampling, resulting in a larger encoded FOV, is also essential for algebraic reconstruction of the dead-time gap, as it ensures that the object has finite support in image space.

The ZTE pulse sequence is designed to be silent, and this is achieved by two essential features: (1) constant gradient FID readout and (2) minimal updates of the readout direction in between repetitions. However, this does not mean that all ZTE acquisitions are necessarily silent, but rather that a ZTE pulse sequence can operate within these constraints. For instance, the ZTE BLAST sequence is not silent due to large gradient steps between readouts. On the other hand, the small change in gradient direction between spokes in RUFIS enables silent acquisition. To achieve complete 3D k-space coverage, the end points of the spokes can be arranged in a spiral pattern, as shown in Figure 2.1B.

The acoustic sound pressure and frequency spectrum produced by a ZTE sequence depend on scan parameters such as the readout bandwidth, TR, and number of spokes in the trajectory, since these parameters affect the absolute gradient amplitude, the duration of each spoke, and the gradient transitions between spokes. With commonly used scan parameters for ZTE, the acoustic noise typically stays within 5 dB of ambient noise levels [23].

### 2.3.3 Image Artifacts

ZTE imaging has several advantages, in addition to being a silent acquisition. The low gradient switching rate in ZTE reduces eddy currents, and with a $\mathrm{TE} = 0$ for FID, there is no time for phase accumulation before the readout, resulting in reduced flow and motion artifacts. However, ZTE is still susceptible to phase accumulation during the readout due to off-resonance effects such as main magnetic field inhomogeneity, tissue susceptibility, and fat-water chemical shift. Chemical shift off-resonance effects can be addressed by using a pixel bandwidth larger than the fat-water chemical shift and using k-space based in-phase and out-of-phase ZTE image decomposition or fat saturation pulses.

A unique feature of ZTE imaging is the dead-time gap, resulting in a spherical region in the center of k-space without acquired valid samples. For conventional gridding reconstruction methods, this gap leads to a slowly varying background signal, rolling off towards the edges of the image, which is most apparent in areas with image intensity close to zero, such as the lateral ventricles, sinuses, and background.

Radial k-space sampling in ZTE is less sensitive to motion during data acquisition due to the repeated sampling and averaging of the k-space center. As a result, motion artefacts appear as localized blurring and streaking instead of coherent ghosting across the imaging field of view as seen in Cartesian acquisitions.

### 2.3.4 Typical Pulse Sequences

The previous section provided an overview of the basic ZTE pulse sequence and its native contrast behaviour. The low flip angle RF excitation and effective $\mathrm{TE} = 0$ of ZTE result in minimal contamination from T2* relaxation, susceptibility artefacts, diffusion, and flow effects, leading to native PD and T1-weighted spoiled gradient recalled echo contrast. However, to make ZTE suitable for clinical applications, additional contrasts beyond PD and T1 are required. This subsection summarizes modifications to the ZTE pulse sequence that enable encoding of additional contrasts through magnetization preparation and gradient echo refocusing.

Magnetization prepared FLASH, as originally described by [26], provides a powerful method to extend the contrast range of SPGR-type sequences beyond native PD and T1 weighting. To achieve this, the acquisition is divided into segments, with each segment beginning with a magnetization preparation (MP) module that modifies the longitudinal magnetization to contain a desired contrast weighting, such as T1, T2, MT, or diffusion. This MP is followed by a certain number of low-FA, short-TR SPGR acquisitions. MP-ZTE offers additional advantages, such as being silent, having $\mathrm{TE} = 0$, and fast scanning with a short TR where most of the time is used for image encoding.

The Looping Star pulse sequence is a gradient echo imaging technique that uses quiet gradient refocusing to produce multiple echoes with T2* contrast. The technique involves a series of FID signals that are generated and gradient refocused in a looping, time multiplexed manner, allowing the acquisition of multiple echoes within a single TR period. This technique is particularly useful for imaging tissues with short T2* values, such as cortical bone or myelin.

In contrast, the ZTE-BURST technique is a multi-echo ZTE sequence that uses a series of non-linear magnetic field gradients to refocus the FID signals and generate multiple echoes with T2* contrast. Unlike the Looping Star sequence, ZTE-BURST is associated with higher acoustic noise due to the use of bipolar gradients for signal refocusing. Despite this drawback, ZTE-BURST has been shown to be effective for imaging tissues with short T2* values and for generating multiple echoes with different T2* contrasts.

# CHAPTER 3

# Model-based Image Reconstruction for Looping-star MRI

The aim of this study was to develop a reconstruction method that more fully models the signals and reconstructs gradient echo (GRE) images without sacrificing the signal to noise ratio and spatial resolution. By modeling the trajectories for every spoke and simplifying the scenario to only echo-in and echo-out mixture, the approach explicitly models the overlapping echoes. After building the overlapping echoes into two system matrix, we use the conjugate gradient algorithm (CG-SENSE) with the non-uniform FFT (NUFFT) to optimize the image reconstruction cost function. The proposed method is demonstrated in phantoms and in-vivo volunteer experiments for 3D, high resolution T2*-weighted imaging and functional MRI tasks. The high resolution protocol exhibits improved spatial resolution and reduced signal loss as a result of less intra-voxel dephasing. The fMRI task shows that the proposed model-based method produced images with reduced artifacts and blurring as well as more stable and prominent time courses. The proposed model-based reconstruction results shows improved spatial resolution and reduced artifacts. The fMRI task shows improved time series and activation map due to the reduced overlapping echoes and under-sampling artifacts.

## 3.1 Introduction

Functional magnetic resonance imaging (fMRI) has evolved into the dominant tool for noninvasive imaging of human brain activity. However, the loud acoustic noise in MRI still remains a problem. For example, acoustic noise can cause discomfort and anxiety in patients [1], especially for certain groups of individuals like children or patients with dementia. Furthermore, acoustic noise is an additional confounding sensory stimulus [2, 3,

---

This chapter based on [22, 27], the author's publication in MRM and ISMRM.

4], and can impact the blood-oxygen level dependent (BOLD) response as a function of both its loudness [5] and duration [6]. There are several ways [7] that acoustic noise can impact fMRI tasks and degrade measured task signals. First, acoustic noise from the scanner stimulates the auditory pathway (including the auditory cortex), reducing sensitivity to experimental stimuli [8]. Second, successfully processing degraded stimuli may require additional executive processes [9] (such as verbal working memory or performance monitoring). Finally, scanner noise may cause participant discomfort and increase attentional demands, even for non-auditory tasks.

Although there are many sources of acoustic noise such as gradient coils, RF pulses, cryogenic pumps, and air circulating systems, the main acoustic noise comes from Lorentz forces caused by rapidly changing currents in the magnetic field gradient coils used primarily for spatial localization [10]. Acoustic noise levels can be reduced by hardware modifications, such as gradient designs and shielding [11], quiet scanning mode provided by the vendors [12], and pulse sequence design [14].

Looping-star [16] is a silent MRI pulse sequence that has been used for quantitative susceptibility mapping (QSM), T2*-weighted imaging and fMRI [17]. It uses multiple RF pulses and slowly varying gradients so the acoustic noise is greatly reduced compared to the standard EPI method. This property makes it well suited for cases where low acoustic noise is required, such as pediatric MRI [18] and auditory fMRI tasks [19]. On the other hand, using multiple RF pulses with repeating slowly varying gradients can complicate k-space trajectories and make the reconstruction problem harder. The problem that leads to the most artifact is called the overlapping-echo effect, caused by signals from multiple excitation pulses being simultaneously present while looping through k-space locations.

Multiple methods have been proposed to reduce the overlapping echo artifacts. The first method [16] assumes that the echo-out and echo-in signal dominates the acquired signal at the beginning and the end of the sampling period, thus separating the overlapping echoes at the cost of lower SNR and spatial resolution. The second method, RF-phase cycling, requires an additional scan with $\pi$ RF phase change and then separates the overlapping echoes by doing a linear combination of signals from these two scans. This method can increase the SNR by a $\sqrt{2}$ at the cost of doubled scan time. The third method [20], coherence-resolved looping-star, uses half as many RF pulses with increased time intervals to separate the echoes. It can be viewed as the same as the standard windowing method, but starting with fewer spokes and a higher resolution input. This method has half as many spokes as the original looping star, so it needs a longer scan time for structural MRI and has worse temporal resolution in fMRI tasks when matching the overall undersampling factor. None of the previous methods can separate the overlapping echoes without sacrificing scan time, spatial resolution, or SNR. In this paper, we propose a model-based reconstruction approach [21] that can theoretically resolve the overlapping echoes and maintain the resolution without increasing the scan time, building on our preliminary work in [27]. Along with the model-based reconstruction method, we used 3D golden-angle-based k-space trajectories [28, 29] for more uniform k-space coverage and reduced under-sampling artifacts.

There are a few reasons to expect that model-based reconstruction can perform better in looping-star MRI. First, the model-based reconstruction method uses more high-frequency data that is filtered out in the gridding reconstruction. Therefore, the image spatial resolution is improved, which can reduce signal loss in T2*-weighted imaging. Secondly, by modeling both echo-in and echo-out signals, the overlapping echoes are mostly resolved, whereas the gridding method neglects either the echo-in or echo-out signal. Thirdly, model-based reconstruction naturally uses the sensitivity maps for SENSE parallel imaging reconstruction [30], reducing undersampling artifacts. Lastly, applying an appropriate regularizer can reduce image noise and improve image quality.

## 3.2 Methods

### 3.2.1 Looping-star physical parameters

The looping-star sequence was developed to acquire $T_2^*$-weighted gradient-echo imaging data while maintaining its quiet performance. We used TOPPE [31] to separately generate excitation and acquisition modules and then combined those modules to form the pulse sequence. Our implementation can be easily extended to other variants of looping star by editing or adding modules. Figure 3.1 illustrates the pulse sequence diagram for looping-star fMRI and the corresponding k-space trajectory. During the first half of the sequence, the radial spokes are excited using a burst of short hard RF pulses [32] with a slowly changing gradient to control the direction of the trajectory. During this part, one can acquire a free-induction-decay (FID) image at TE $\approx 0$, though we did not use the FID data for the current work. The second half of the sequence applies the same gradient again but without RF pulses to create the gradient echo (GRE) signal used to produce a gradient echo image at TE = 27.67 msec, which is expected to give sufficient functional BOLD contrast at 3T. Each RF subpulse produces a low-frequency line thorough the center of k-space; the collection encodes a disk in 3D k-space, and this gradient encoding can be repeated additional times for multiple GRE echoes. We generate the full 3D trajectory by rotating the 2D k-space trajectories.

### 3.2.2 Acquisition Method

We designed several protocols for different needs including a hi-res protocol for structural imaging, and mid-res and low-res protocols for fMRI studies.

For structural imaging, we use 12 RF pulses with 2.24ms readout per RF pulse to achieve about 1.25 mm isotropic resolution, which we call the high-resolution protocol. Two GRE echoes are collected to acquire images with TE $= 27.67$ms and TE $= 54.55$ms. For multiple GRE echoes, we define a separate forward model for each echo and reconstruct each echo independently. For fMRI studies, we designed two protocols with different spatial and temporal resolution. We found that an odd number of RF pulses produced more uniform 2D k-space coverage in the highly undersampled fMRI cases, so we used 23 RF pulses with 1.12ms readout per RF pulse in mid-res protocol to achieve 3mm isotropic spatial resolution and 3.6s temporal resolution, and 31 RF pulses with 0.84ms readout per RF pulse for low resolution protocol to achieve 3.75mm isotropic spatial resolution and 1.8s temporal resolution. The RF pulse interval and gradient waveforms were adjusted such that the echo time is approximately 27.67ms for both protocols. To produce an excitation profile that is as uniform as possible, we used a series of very short 12$\mu$s RF pulses with near maximum magnitude in the excitation module with a flip angle of 3°.

For all protocols, we first designed a 2D sinusoidal gradient with acquisition dwell time of 4$\mu$s, a maximum gradient amplitude of 5 mT/m and maximum slew rate of 1 mT/m/ms in terms of the root sum of square of x and y axes. Then in 3D, to achieve more uniform k-space spokes, we adopted the 3D golden-angle based rotation [33] by generating a series of azimuth and polar angles with small increment. The 2D k-space trajectories were rotated along x axis by the azimuth angle and along the z axis by polar angle. We used 4800 3D rotations in hi-res protocol, 64 and 32 3D rotations for each time frame in mid-res and low-res fMRI protocols respectively. The structural and fMRI protocols are tested in phantom and in-vivo studies.

Because TOPPE currently requires the gradient of each module to start and end at zero, we used ramp-up and ramp-down gradients before and after the excitation and acquisition module to accommodate this constraint. The max slew rate of the ramp up and ramp down gradient was set to 5 mT/m/ms.

Sensitivity maps were estimated from a 2 minute 3D GRE pulse sequence with 3mm isotropic spatial resolution.

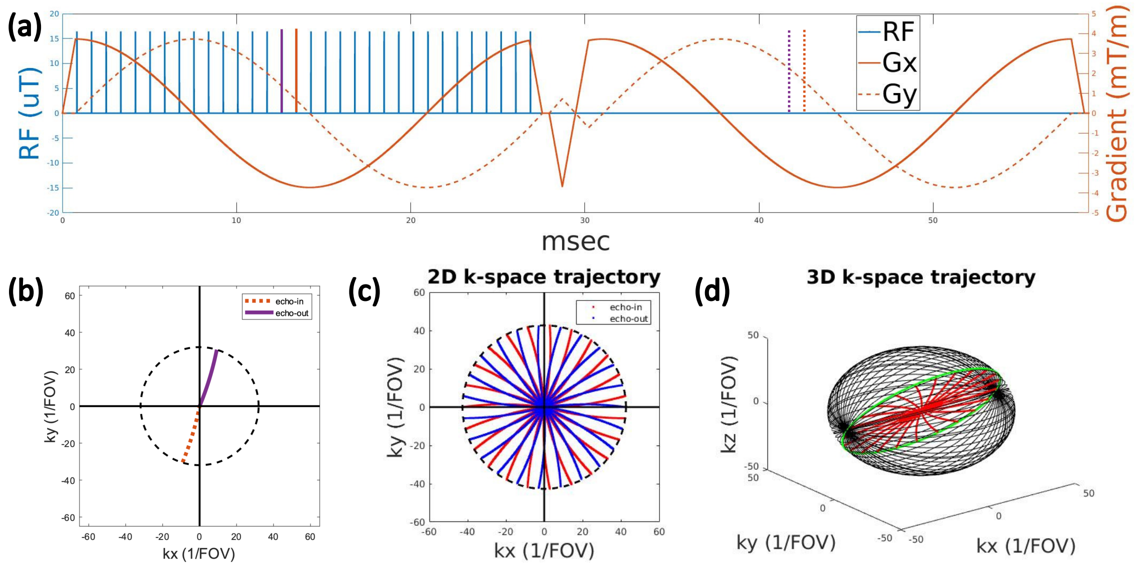

**FIG** 3.1 – (a) A pulse sequence for a 2D plane of the 3D acquisition with one excitation/FID module and one GRE/data acquisition module (ramp-up and ramp-down gradient are required by TOPPE), the max slew rate for all modules (including ramps) is 5 mT/m/ms; (b) Illustration of overlapping echoes in GREmodule: the echo-out signal from purple RF pulse overlaps the echo-in signal from orange RF pulse in time; (c) 2D GRE k-space trajectory: an odd number of spokes generates more evenly distributed spokes; (d) 3D k-space trajectory using 3D generalized golden-angle.

### 3.2.3 Signal models in looping-star

In model-based reconstruction [21], we approximate the object magnetization $f(\vec{r})$ using a finite series expansion as follows

$$f(\vec{r}) = \sum_{n=0}^{N-1} f_n \, b(\vec{r} - \vec{r}_n), \tag{3.1}$$

where $b(\cdot)$ denotes the object basis function, typically a voxel indicator function, $\vec{r}_n$ denotes the center of $n$th translated basis function, and $N$ is the number of parameters (voxels).

In looping-star fMRI, assuming we have $N_{\text{rf}}$ RF pulses in one cycle of FID and following GRE, there will be up to $N_{\text{rf}}$ k-space trajectories, each corresponding to a previously applied RF pulse. Therefore, the GRE signal sampled at any time $t$ is a superposition of $N_{\text{rf}}$ k-space samples located on corresponding trajectories.

The corresponding signal equation for the $\imath$th spoke ($i = 1, \ldots, N_{\mathrm{rf}}$) and $\jmath$th receiver coil ($j = 1, \ldots, J$) is given by [21]

$$s_{ij}(t) = \int c_j(\vec{r}) f(\vec{r}) \left( \sum_{l=1}^{N_{\mathrm{rf}}} \mathrm{e}^{-z(\vec{r})(t+(i-l)\Delta t)} \, \mathrm{e}^{-\imath 2\pi \vec{k}_l(t+(i-l)\Delta t)\cdot \vec{r}} \right) d\vec{r}, \tag{3.2}$$

where a continuous time index $t$ is the time for the $\imath$th spoke starting from the end of the $\imath$th RF pulse, $c_j(\vec{r})$ is the sensitivity map of $\jmath$th receiver coil, $f(\vec{r})$ is the unknown continuous complex transverse magnetization, $z(\vec{r}) \triangleq 1/T_2^*(\vec{r}) + \imath \Delta\omega_0(\vec{r})$ is the "rate map", $\Delta t$ is the time interval between adjacent RF pulses, $(i-l)\Delta t$ is the time between the $\imath$th and $l$th RF pulse, and $\vec{k}_l(t)$ is the k-space trajectory for the $l$th RF pulse at time $t$.

Each $l$ represents a RF pulse that contributes to the signal. When $l = i$, the corresponding k-space trajectory $\vec{k}_i(t)$ moves from the center k-space to outer k-space, which is called echo-out trajectory, and when $l = i + 1$, the corresponding k-space trajectory $\vec{k}_{i+1}(t - \Delta t)$ moves from the outer k-space to center k-space, which is called echo-in trajectory.

After space discretization [34] using (3.1), we approximate (3.2) by

$$\begin{aligned} s_{ij}(t) = \sum_{l=1}^{N_{\mathrm{rf}}} & B(\vec{k}_l(t + (i-l)\Delta t)) \\ & \sum_{n=0}^{N-1} c_j(\vec{r}_n) f(\vec{r}_n) \, \mathrm{e}^{-z(\vec{r}_n)(t+(i-l)\Delta t)} \, \mathrm{e}^{-\imath 2\pi \vec{k}_l(t+(i-l)\Delta t)\cdot \vec{r}_n}, \end{aligned} \tag{3.3}$$

where $B(\vec{k}(\cdot))$ denotes the spectrum of the object basis function $b(\cdot)$.

We express the noisy measured signals for $\imath$th spoke and $\jmath$th coil in matrix-vector form as follows

$$\boldsymbol{s}_{ij} = \left( \sum_{l=1}^{N_{\mathrm{rf}}} \boldsymbol{A}_{il} \right) \boldsymbol{C}_j \boldsymbol{f} + \boldsymbol{\epsilon}_{ij} \in \mathbb{C}^M, \tag{3.4}$$

where $\boldsymbol{f} = (f_1, \ldots, f_N)$ is the vector of parameters (voxel values) we hope to estimate from the measurement $\boldsymbol{s}$, $\boldsymbol{C}_j \in \mathbb{C}^{N \times N}$ is the diagonal sensitivity map matrix, and each element of the matrix $\boldsymbol{A}_{il} \in \mathbb{C}^{M \times N}$ is given by

$$\begin{aligned} a_{ilmn} = & B(\vec{k}_l(t_m + (i-l)\Delta t)) \\ & \mathrm{e}^{-z(\vec{r}_n)(t_m+(i-l)\Delta t)} \, \mathrm{e}^{-\imath 2\pi \vec{k}_l(t_m+(i-l)\Delta t)\cdot \vec{r}_n}, \end{aligned} \tag{3.5}$$

where $i$ is the spoke index, $j$ is the coil index, $l$ is the RF pulse index, $m$ is the index for a discrete time point in k-space, and $n$ is the index for discrete image grid.

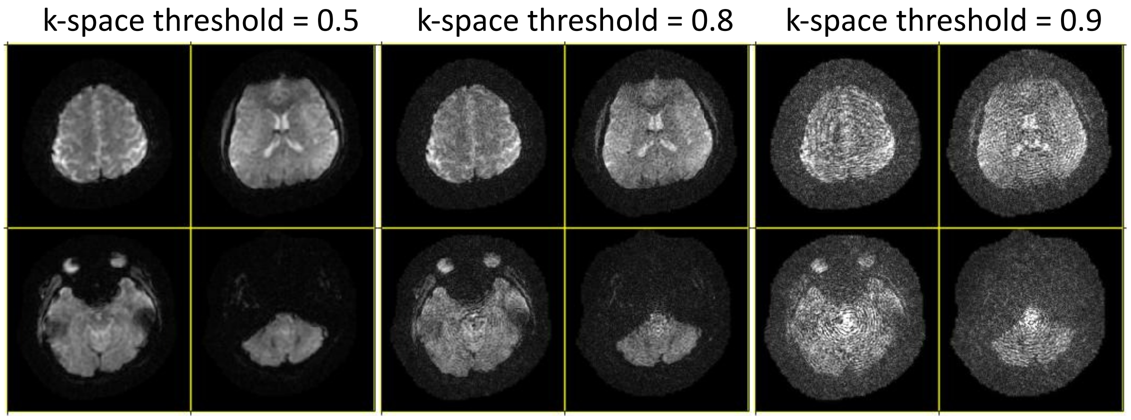

FIG 3.2 – Overlapping echo artifact from the conventional gridding methods. As the k-space cut-off increases, the overlapping echo artifact can significantly degrade the image quality.

Stacking up all $J$ measurement vectors and sensitivity map matrices from all coils and defining the system matrix for the $i$th echo to be $\boldsymbol{A}_i = \sum_{l=1}^{N_{\text{rf}}} \boldsymbol{A}_{il} \in \mathbb{C}^{M \times N}$ yields the linear model

$$\boldsymbol{s}_i = (\boldsymbol{I}_J \otimes \boldsymbol{A}_i)\, \boldsymbol{C}\boldsymbol{f} + \boldsymbol{\epsilon}_i, \tag{3.6}$$

where $M$ is the number of samples per spoke, $\boldsymbol{C} = [\boldsymbol{C}_1; \ldots; \boldsymbol{C}_J] \in \mathbb{C}^{(JN) \times N}$, $\boldsymbol{I}_J$ is a $J \times J$ identity matrix, and $\otimes$ denotes the Kronecker product.

To perfectly model all the spokes, the optimal signal model would take all those k-space locations into account. However, modeling all the spokes would require approximately 512 cubic spatial resolution and in practice is computationally infeasible, especially in fMRI scans with many time frames. Our implementation simplifies the signal model to include only signals from echo-in spokes and echo-out spokes. Specifically, we simplify (3.6) to

$$\boldsymbol{s}_i = (\boldsymbol{I}_J \otimes \tilde{\boldsymbol{A}}_i)\, \boldsymbol{C}\boldsymbol{f} + \boldsymbol{\epsilon}_i, \tag{3.7}$$

where we use the two-term approximation $\tilde{\boldsymbol{A}}_i = \sum_{l \in \{i, i+1\}} \boldsymbol{A}_{il}$. Here $l = i + 1$ corresponds to the echo-in spoke and $l = i$ corresponds to the echo-out spoke.

Two special cases are the first and last spokes, where an FID overlaps with a first gradient echo or an recalled gradient echo overlaps with a later gradient recalled echo, which are problematic due to the unknown $T_2^*$ map and disparate signal strengths. These cases are eliminated from the system model by setting $i = 1, ..., N_{\text{rf}} - 1$.

### 3.2.4 Model-based reconstruction

With above discrete system matrix, we use the conjugate gradient method to optimize the following cost function

$$\hat{\boldsymbol{f}} = \arg\min_{\boldsymbol{f}} \|\boldsymbol{s} - \boldsymbol{A}\boldsymbol{C}\boldsymbol{f}\|_2^2 + \beta R(\boldsymbol{f}), \tag{3.8}$$

where $\boldsymbol{s} = [\boldsymbol{s}_1; \ldots; \boldsymbol{s}_{N_{\text{rf}}}]$ is the vertically stacked signal, $\boldsymbol{A} = [(\boldsymbol{I} \otimes \tilde{\boldsymbol{A}}_1); \ldots; (\boldsymbol{I} \otimes \tilde{\boldsymbol{A}}_{N_{\text{rf}}})]$ is the stacked system matrix, and $R(\boldsymbol{f}) = \|\boldsymbol{D}f\|_2^2$ is a 3D roughness regularizer using quadratic 1st-order finite differences with 26 neighbors. We use CG-SENSE [30] with 30 iterations to optimize (3.8).

### 3.2.5 k-space filtering and object basis spectrum

For gridding reconstruction of all protocols, a hard cut-off was used to truncate the k-space data with a k-space window at 50% (unless specified otherwise) to reduce the overlapping echo artifact [17].

For model-based reconstruction, instead of filtering out the mixed signals, we model the echo-in and echo-out mixture using an object basis function whose spectrum $B(\boldsymbol{k})$ is Fermi shaped with a cutoff frequency around 90%. We use this 90% cutoff frequency because the magnitude of low-frequency components near the k-space origin is much larger than the magnitude of the high-frequency components; therefore when these two signals are superimposed, it is very difficult to recover the high-frequency components accurately. Section S.1 of the supplement gives details about choosing the object basis function.

### 3.2.6 Implementation and reproducible research

The reconstruction code is available at `https://github.com/haoweix/MBLS`, ensuring the reproducibility of the computational aspects of our research. For pulse programming, we used TOPPE [31] to implement the looping-star pulse sequence on a GE UHP 3.0T scanner with a Nova Medical 32-channel Rx head coil. For model-based reconstruction, we used the Matlab toolbox MIRT [35] to build the NUFFT-based system matrix and optimize the cost function.

We compared the proposed model-based reconstruction using echo-in and echo-out system matrices (MB-2 in figures below) to a simpler model-based reconstruction method that used a single echo-out system matrix, $A_1$ (MB-1 in figures below) and a gridding method that used a density compensation function and a gridding over-sampling factor of 2. Then we applied sensitivity map based complex coil combination to construct the final images. We tested the structural MRI protocol on 3 subjects and variants of the fMRI protocol on 4 subjects. Subjects gave informed consent under IRB approval from the University of Michigan.

## 3.3 Results

We demonstrated proposed model-based reconstruction approach on phantom and in-vivo scans.

### 3.3.1 Acoustic noise level

We measured the acoustic noise by placing a phone (iPhone SE) in the scan room and using a phone app (NIOSH Sound Level Meter Version 1.2.6) to record 30s of the noise, then computing the sound level. Without playing any pulse sequence, the ambient noise levels were 59.3 dB LAeq and 83.0 dB LCpeak. LAeq is the average sound level over the recorded period, representing the continuous equivalent noise level, while LCpeak is the highest noise level recorded during that period. The multi-band EPI, a typical fMRI pulse sequence, produced noise levels of 97.4 dB LAeq and 105.6 dB LCpeak. In contrast, the looping-star sequence had noise levels of 60.7 dB LAeq and 84.7 dB LCpeak. The acoustic noise of the looping-star sequence is, on average, approximately 1.4 dB higher than the ambient noise but reduces the noise by 36.7 dB compared to the commonly used multi-band EPI sequence.

### 3.3.2 Overlapping echo artifacts demonstration

Figure 3.2 illustrates the resultant effect for overlap of the echo-in and echo-out spokes in the gridding reconstruction. For k-space filter with a threshold of 0.5, there is little artifact, but resolution is lowered by roughly a factor or two in all three directions. For higher cutoffs, there is a tradeoff between spatial resolution and artifact resulting from misassigned spatial frequency components.

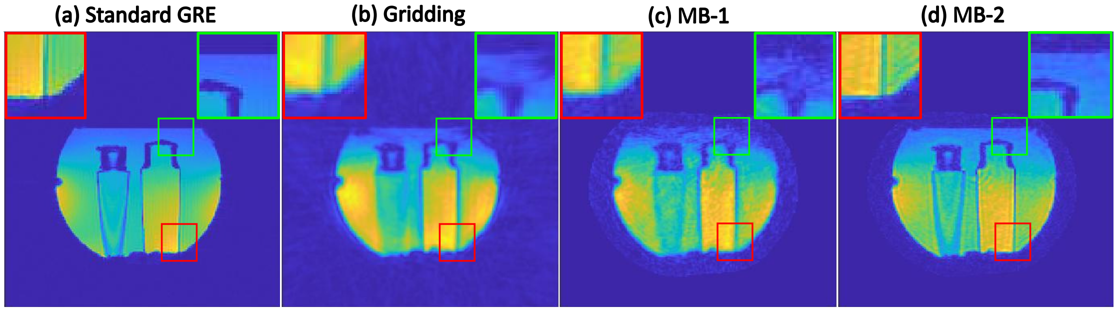

**FIG** 3.3 – Hi-resolution looping-star reconstruction in phantom study. (a) standard $T_2^*$-weighted GRE (scan time: 21 min); (b) Gridding reconstruction with density compensation function; (c) MB-1 without overlapping echo modeling; (d) MB-2 with overlapping echo modeling. For (b) (c) (d), all use the same k-space data with scan time of about 7 minutes. (d) shows similar spatial resolution (slightly reduced due to voxel indicator function and spherical acquisition pattern) to the standard GRE , and improved image quality compared to (b) and (c) in terms of sharper edges (red zoom-in box) and recovered signal loss (green zoom-in box).

### 3.3.3 Phantom experiments

Figure 3.3 shows the reconstruction for structured phantom using a hi-resolution looping-star protocol. We compare the results of standard gradient echo acquisition with standard FFT reconstruction to looping-star reconstruction using gridding, model-based reconstruction without modeling overlapping signal (MB-1), and model-based method with overlapping signal modeling (MB-2). MB-2 significantly improved the spatial resolution by modeling the high-frequency components in sampled signals compared to the gridding method. Signal loss near the phantom-air edges is also recovered due to the spatial resolution improvement.

### 3.3.4 In-vivo experiments

The proposed method reduced the overlapping echo artifacts and improved the spatial-temporal resolution in both structural and functional MRI, compared to the conventional gridding method.

#### 3.3.4.1 Structural MRI

Figure 3.4 shows the reconstruction for a human brain scan in a representative subject using the high-resolution protocol (1.25mm isotropic). The structural MRI results using

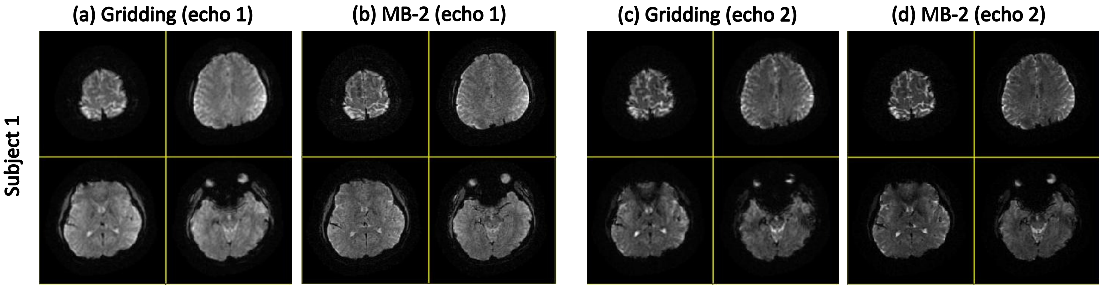

**FIG** 3.4 – Hi-resolution looping star reconstruction for a representative subject. MB-2 provided improved spatial resolution and recovered signal loss, particularly in the inferior slices for echo 2, compared to gridding reconstruction.

hi-res protocol for the other 2 subjects are shown in figure S1 to further support the increased spatial resolution compared to the gridding method. For the gridding method, overlapping echo artifact was reduced by truncating the k-space, which also reduced the spatial resolution. The proposed MB-2 shows increased spatial resolution, reduced overlapping echo artifacts as well as improved image quality, compared to the gridding method. Besides the sharper images, the signal loss around frontal sinuses and ear canals is recovered due to the smaller voxel size. Due to almost halved spatial resolution, the gridding method has a 4X lower (better) undersampling rate than the MB-2 method. MB-2 method has higher undersampling rate and thus potentially more affected by the undersampling artifact even with Model-based reconstruction method. The reconstructions from other 2 subjects in Figure S1 support that MB-2 improves the spatial resolution by almost a factor of 2 and the circular ringing artifacts in the top right slices of subject 1 might have come from motion or other factors.

### 3.3.4.2 Functional MRI

We demonstrated application of the proposed methods to fMRI by doing finger-tapping and visual fMRI tasks. In the fMRI study, healthy participants watched a flashing checkerboard for multiple cycles (20s on and 20s off), and were required to tap their fingers while the checkerboard was on. Figure 3.5 shows the activation map and time course for the finger-tapping test in a typical subject. The proposed MB-2 reconstruction method showed higher correlation and less noise on the activation map as compared to gridding method. Its time course also better matches the task reference and is less noisy.

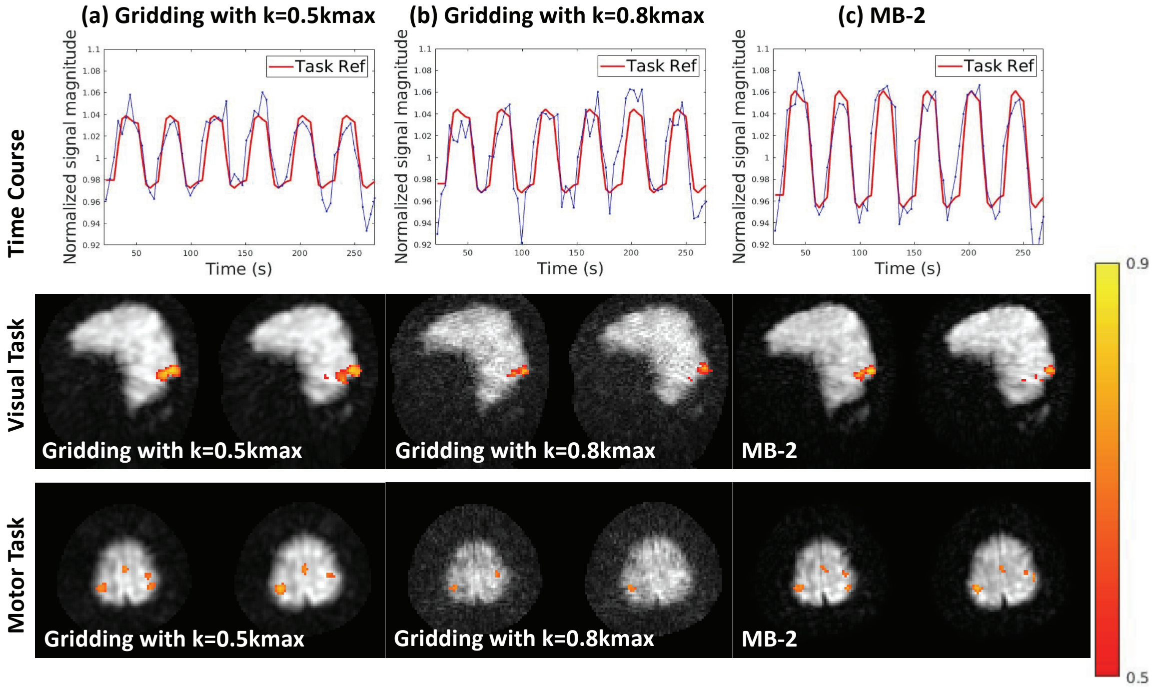

**FIG** 3.5 – fMRI task result. First row: time course from the voxel with the highest correlation coefficient. With the improved spatial resolution, time course in MB-2 shows larger signal change due to the reduced partial volume effect. Second row: sagittal activation map for visual tasks (two consecutive slices). Although the undersampling artifact (20x undersampled) dominates the artifacts here, MB-2 reconstruction still shows slightly improved spatial resolution. With gridding method, activation map is smoothed and potentially showing false positives. Third row: Axial activation map for finger-tapping tasks (two consecutive slices).

## 3.4 Discussion

Compared to the standard GRE method, the biggest disadvantage of looping-star is the low SNR that limits its spatial and temporal resolution. By exploiting the high-frequency k-space information, the proposed method can resolve the overlapping echoes and use about twice as many signal samples for reconstruction, which also improves the SNR by a factor of nearly $\sqrt{2}$. However, since the high-frequency signal values are mixed with the low-frequency signals, which have a much larger magnitude, it is difficult to accurately estimate the highest-frequency components. To overcome this problem, we used a object basis spectrum based on a Fermi function that effectively leads to a slight truncation of the high-frequency components (≈90%) at the end of the echo-in and echo-out spokes acquisition. This approach reduced the image distortion coming from the mis-estimation of the highest-frequency signals.

One other reconstruction method RF-cycling[16] leads to reduced temporal resolution. Another approach is coherence-resolved looping-star [20], which removes most of the overlapping echo artifacts by pushing further in k-space before the next RF pulse is applied. This by done by increasing the gradient strength for a fixed number of RF pulses, thus increasing acquisition bandwidth, resulting in reduced SNR. Alternatively, the coherence-resolved approach can be implemented by reducing the number of RF pulses, which can maintain the SNR, but increases undersampling artifact by reducing the number of spokes. In all of these approaches [20, 17], there is a loss of image quality, SNR or temporal resolution.

For the excitation process, considering the typical T1 value of the gray matter and 23 RF pulse of 3 degree flip angle and using small tip angle approximation, the Mz of the last RF pulse was about 3.2% decreased compared to the first RF pulse for gray matter. Therefore, we neglected the impact of the Mz decrease in our signal model. RF-induced echo splitting and resulting higher-order echoes (spin-echoes, stimulated echoes, etc) are neglected, again, because of the low FAs [16]. In addition, the higher-order echoes are also not re-phased in the gradient-echo module due to the continuously changing gradient fields.

We used 3D golden-angle based sampling trajectories to achieve more uniformly distributed spokes. The performance of randomly rotated spokes highly depends on the random seed, so the image quality in each frame of fMRI studies would differ significantly if different sampling patterns for each frame were used. Accordingly, we repeated the a single 3D pattern for all fMRI temporal frames.

One potential issue with the proposed approach is whether poor conditioning could lead to noise amplification in the reconstruction. The standard deviation maps in Figure S2 show that the model using echo-in and echo-out system matrices have nearly identical reconstruction noise relative to the model using echo-in system matrix only.

The actual spatial resolution in reconstructed images is related to the regularization parameters when using roughness and many other regularizers. Therefore, regularization parameters need to be chosen carefully here as one of the main goals for using model-based reconstruction is to improve spatial resolution. Section S.2 and Figure S3 of the supplementary material give details about choosing regularization parameters and quantifying the spatial resolution.

The traditional gridding method either suffers from low-spatial resolution and reduced signal change due to partial volume effects by truncating too much (truncation to $0.5k_{max}$), or suffers from overlapping echo artifacts and more noise by truncating too little. The proposed MB-2 method resolves the overlapping echoes and showed improved spatial resolution (about 1.8x expected relative to the lower resolution gridding), larger signal change, and better activation compared to previous methods. The longer effective readouts for MB-2 can improve the SNR by a factor of $\sqrt{1.8}$, thus leading to a net SNR reduction of $\frac{\sqrt{1.8}}{1.8^3}$ compared to the gridding method, where the $1.8^3$ comes from the reduced 3D voxel size. Still, the FMRI results did not appear to be limited by thermal noise. Quantifying spatial resolution and SNR will be part of our future work.

There are several other directions for improving image quality and SNR in future work. These include shaped RF pulses to reduced hard pulse shading across the field of view and variable flip angles schemes to maximize signal strength and uniformity. We will also consider approaches to optimize the sampling pattern using learning-based method to further reduce image artifacts and increase image qualities [36]. For multi-echo looping-star, learning-based networks can provide fast and accurate quantitative $T_2^*$ mapping [37]. We will also further explore the possibility of using spatial-temporal reconstruction model in looping-star [38].

## 3.5 Conclusion

We proposed a novel model-based reconstruction method to resolve the overlapping echo challenge in looping-star pulse sequences. We also used a 3D golden-angle based sampling pattern and mid-resolution fMRI protocol to further improve the image quality in the fMRI studies. By exploiting the high-frequency k-space information, the proposed approach was able to recover high-resolution images and reduce the artifacts compared to previous methods, while preserving the temporal resolution in fMRI.

## 3.6 Supplementary material

### 3.6.1 Object basis function

The Fermi filters must be applied to each sub-system matrix individually before matrix combination because the echo-in and echo-out signals need to be filtered in ‘opposite’ directions. One cannot apply two different filters directly to the data.

The exact shape of the spectrum of object basis function $B(k)$ depends on the pulse sequence parameters, such as the spatial resolution and number of spokes. Empirically, we chose a 90% cutoff frequency to reduce the mixture of center k-space signals and high-frequency signals coming from the echo-in and echo-out spokes respectively. We then chose the transition band to reduce the ringing artifact that would be caused by a hard cutoff.

### 3.6.2 Spatial resolution

The actual spatial resolution in reconstructed images is related to the regularization parameters when using roughness and many other regularizers. Therefore, regularization parameters need to be chosen carefully here as one of the main goals for using model-based reconstruction is to improve spatial resolution.

Here we empirically chose the regularization factors such that undersampling artifact can be mitigated while preserving most of the spatial resolution. We report the full width at half maximum (FWHM) values and corresponding regularization factors here to help understand the relationship between spatial resolution and regularization factors. Fig. 3.8 shows the FWHM of the point spread function (PSF) over iterations and the reconstructed images at 30 and 100 iterations. The FWHM of MB-2 method is about 2.5 pixels at 50 iteration and the FWHM of gridding method is about 3.6 pixels.

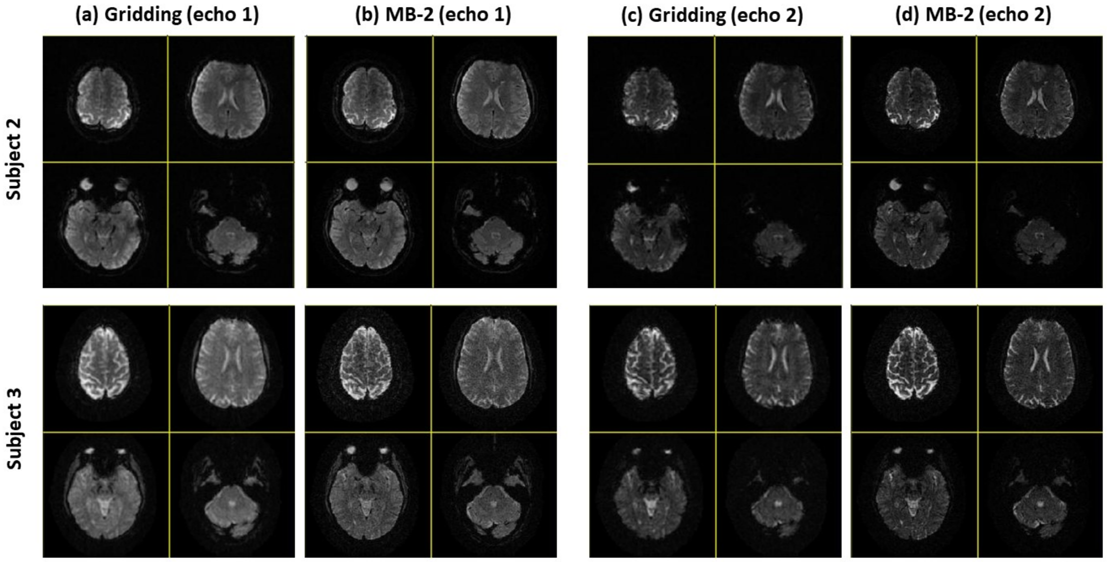

**FIG** 3.6 – Hi-resolution looping star reconstruction for two additional subjects. The proposed MB-2 approach provided improved spatial resolution and recovered signal loss in multiple areas compared to gridding reconstruction.

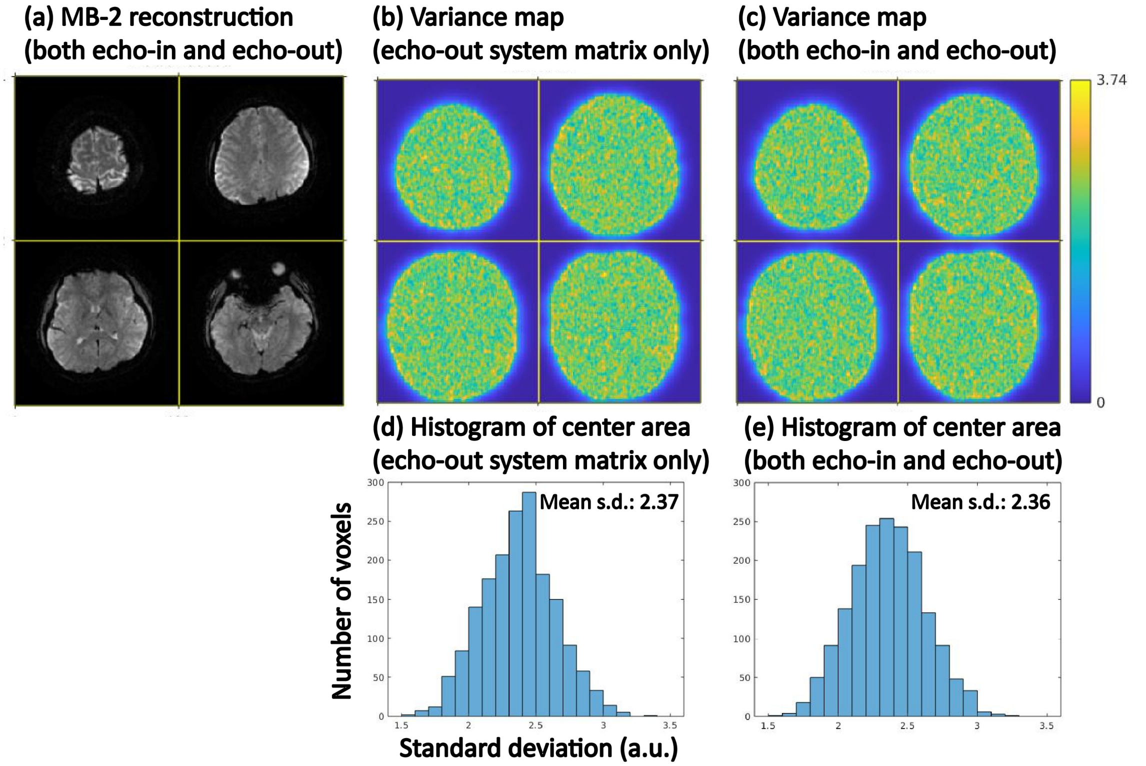

**FIG** 3.7 – Reconstruction and variance maps. (a) shows the hi-resolution reconstruction for references. (b) and (c) are the standard deviation maps using echo-out system matrix only and both echo-in and echo-out system matrices respectively. (d) and (e) are corresponding histogram of these 4 slices. We generated standard deviation maps, estimated from 20 realizations of additive complex white Gaussian noise to the measured signal in the fMRI protocol. The model using echo-in and echo-out system matrices have nearly identical reconstruction noise relative to the model using echo-in system matrix only, indicating that using echo-in and echo-out system matrices does not worsen the conditioning or the noise amplification for the regularization parameters used in this work.

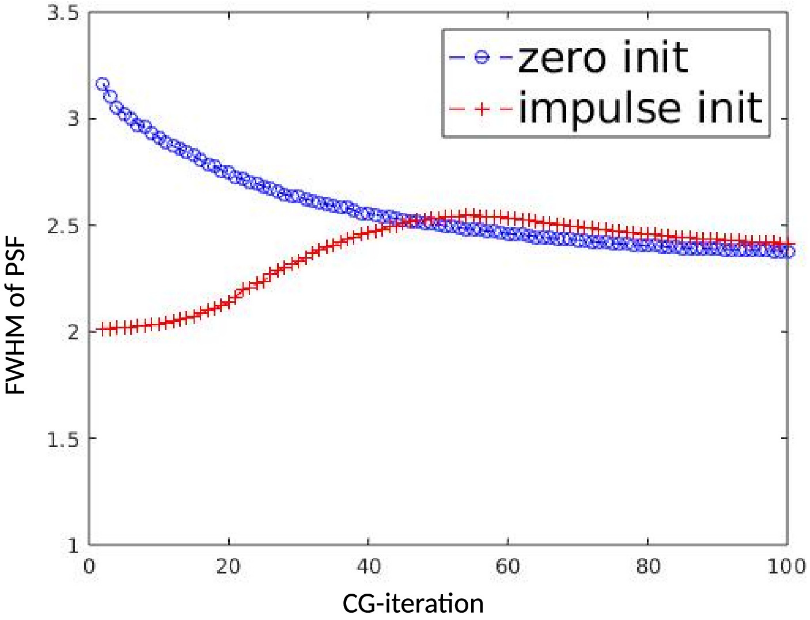

(a) FWHM of PSF over iterations

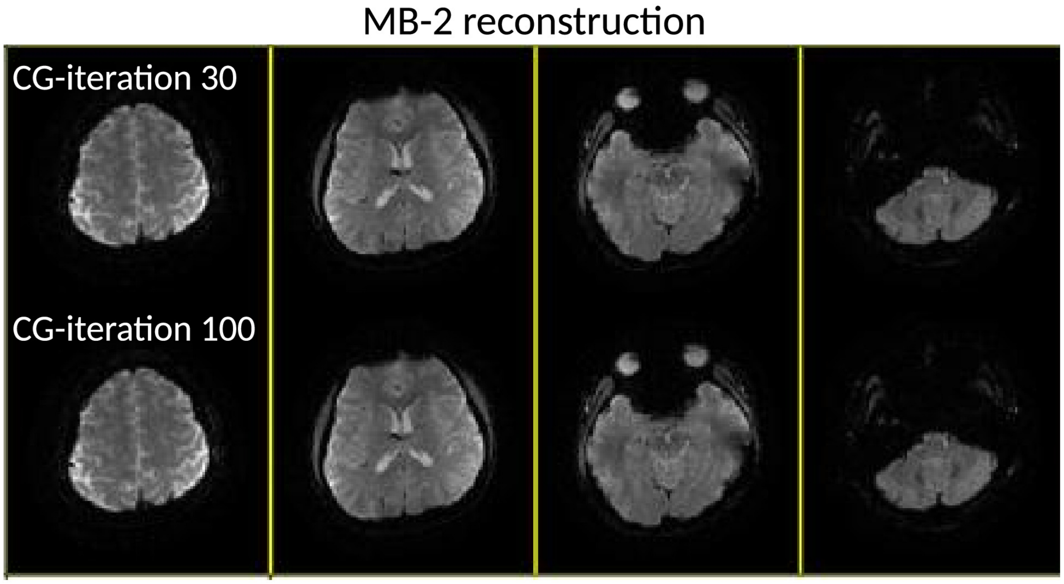

(b) MB-2 reconstruction at different iterations

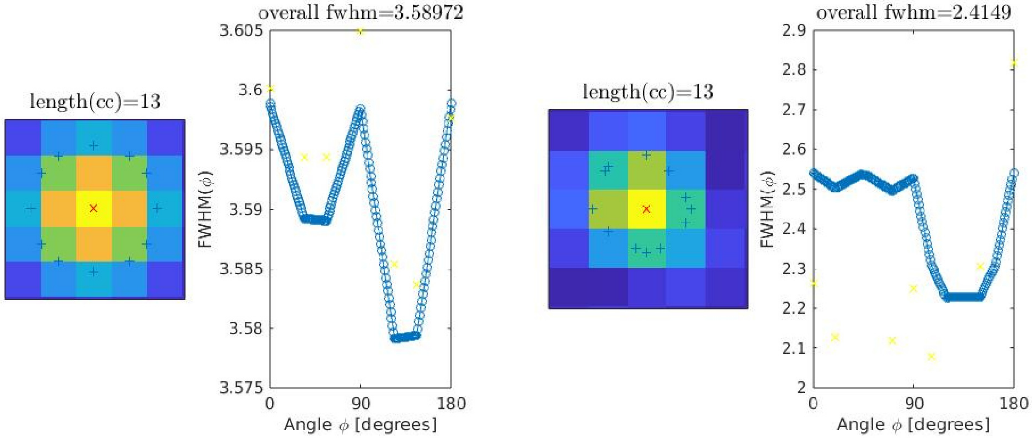

PSF from gridding

PSF from MB-2

(c) PSF comparison between gridding and MB-2

**FIG** 3.8 – FWHM of PSF over iterations and MB-2 reconstruction at different iteration. (a) shows the FWHM of PSF over CG-iterations. The FWHM of PSF is computed by reconstructing the k-space data of a Kronecker impulse function. The PSF gradually converged after 50 iterations. (b) shows the MB-2 reconstructions of the same subject at iteration 30 and 100 with zero initialization. Though the PSF still decreases after 30 iterations, the change in the reconstructed images is non-visible, so for most of the results shown in the paper, we stopped at 30 iteration to save compute time. The FWHM of PSF using gridding method is measured to be 3.59 pixels for comparison. (c) compares the PSF from the center slice of the subject. The curve shows the radial FWHM of all direction and the overall FWHM is the averaged value.

## CHAPTER 4

# Spatial-temporal Reconstruction for Looping-star MRI using UNFOLD and LLR

## 4.1 Introduction

Functional magnetic resonance imaging (FMRI) has become the leading method for noninvasive imaging of human brain activity. However, the issue of loud acoustic noise in MRI persists. This noise can cause discomfort and anxiety in patients [1], especially in vulnerable populations such as children or those with dementia. Additionally, acoustic noise acts as an extraneous sensory stimulus [2, 3, 4], potentially affecting the blood-oxygen level dependent (BOLD) response depending on its loudness [5] and duration [6]. There are several mechanisms [7] through which acoustic noise can impact fMRI tasks and degrade the quality of measured signals. Firstly, scanner noise stimulates the auditory pathway, including the auditory cortex, reducing sensitivity to experimental stimuli [8]. Secondly, processing degraded stimuli may require additional cognitive processes [9], such as verbal working memory or performance monitoring. Lastly, scanner noise can cause participant discomfort and increase attentional demands, even during non-auditory tasks.

Acoustic noise in MRI arises from multiple sources, including gradient coils, RF pulses, cryogenic pumps, and air circulating systems. The primary source of this noise is the Lorentz forces generated by rapidly changing currents in the magnetic field gradient coils used for spatial localization [10]. Acoustic noise levels can be mitigated through hardware modifications, such as optimized gradient designs and shielding [11], the implementation of quiet scanning modes provided by vendors [12], and the development of specific pulse sequence designs [14].

Looping-star pulse sequence [16] is a silent MRI method used for quantitative susceptibility mapping (QSM), T2*-weighted imaging, and fMRI [17]. It employs multiple RF pulses

---

This chapter extends the author's published work at ISMRM 2023 [38].

and slowly varying gradients, significantly reducing acoustic noise compared to the standard EPI method. This characteristic makes it ideal for situations where low acoustic noise is essential, such as pediatric MRI [18] and auditory fMRI tasks [19]. However, using multiple RF pulses with repeating slowly varying gradients can complicate k-space trajectories and make the reconstruction process more challenging. The most significant artifact issue, known as the overlapping-echo effect, is caused by signals from multiple excitation pulses being present simultaneously while traversing k-space locations.

Compressed sensing (CS) is a powerful technique used in MRI to increase imaging speed and efficiency and overcome some of the major limitations in terms of spatial and temporal resolution, volumetric coverage, and sensitivity to motion. This technique takes advantage of the fact that medical images are naturally compressible in some appropriate basis, such as wavelets, finite differences, or learned dictionaries.

MRI data are acquired in the spatial frequency domain (k-space) rather than in the image domain, which facilitates the generation of incoherent aliasing artifacts via random undersampling of Cartesian k-space or the use of non Cartesian k-space trajectories. Image reconstruction is performed by enforcing sparsity in the solution, subject to data consistency constraints. CS can be combined with parallel imaging to further increase imaging speed by exploiting joint sparsity in the multi-coil image ensemble.

Dynamic MRI is particularly well suited for the application of CS due to extensive spatial-temporal correlations that result in sparser representations than would be obtained by exploiting spatial correlations alone. The successful application of CS requires image sparsity and incoherence between the acquisition space and representation space.

Spatial-temporal reconstruction is a technique used in dynamic MRI to enhance the quality and resolution of images. Instead of reconstructing each time frame independently, it involves using advanced algorithms to combine data sampled over time to jointly create a series of high-quality images.

The idea behind spatial-temporal reconstruction is that by sharing data over time, it is possible to fill in missing k-space information and overcome limitations in resolution and signal-to-noise ratio that may occur in individual time frame. This is particularly important in dynamic MRI, where image quality can be affected by factors such as undersampling artifact, patient motion, magnetic field inhomogeneities, and other artifacts.

Spatial-temporal reconstruction algorithms use a variety of techniques to combine data over time. These can include low rank models, sparsity in image or other domain, and wavelet analysis. By using these techniques, spatial-temporal reconstruction can yield a series of high-quality images that represent a more accurate representation of the underlying dynamic process. Using spatial-temporal reconstruction algorithms also can improve the trade-off between spatial resolution and temporal resolution that is present in all dynamic MRI scans.

Previous spatial-temporal reconstruction approaches for FMRI have utilized models such as low-rank [39] and low-rank plus sparse [40]. These models impose low-rankness and/or sparsity on matrices of the vectorized space dimension and time. The Locally Low-Rank (LLR) model offers an advantage in preserving local structures within the image. It operates under the assumption that small patches or blocks of the space-time image series are low-rank, which facilitates the capture of local features and details. Conversely, the Global Low-Rank (GLR) model applies a low-rank constraint to the entire image, which can lead to over-smoothing of local structures.

Furthermore, the LLR model provides greater flexibility in data modeling. It can be integrated with other constraints or regularization terms, such as sparsity and smoothness, to more effectively capture the underlying characteristics of the MRI data. In our findings, the locally low-rank model is particularly well-suited for fMRI protocols using the looping-star technique.

## 4.2 Methods

### 4.2.1 Looping-star physical parameters

The looping-star sequence was developed to capture $T_2^*$-weighted gradient-echo imaging data while maintaining a quiet performance profile. We utilized TOPPE [31] to individually generate excitation and acquisition modules, that were then combined to form the complete pulse sequence. Our implementation is flexible and can be extended to other looping-star variants by modifying or adding modules. Figure 3.1 depicts the pulse sequence diagram for looping-star fMRI and its corresponding k-space trajectory.

In the first half of the sequence, radial spokes are excited using a burst of short hard RF pulses [32], with a slowly changing gradient to steer the trajectory direction. During this phase, a free-induction-decay (FID) image can be acquired at TE $\approx 0$, although we did not utilize the FID data for the work presented in this chapter. The second half of the sequence re-applies the same gradient without RF pulses to generate the gradient echo (GRE) signal, producing a gradient echo image at TE = 27.67 msec, which is sufficient for functional BOLD contrast at 3T. Each RF subpulse encodes a low-frequency line through the center of k-space, collectively encoding a disk in 3D k-space. This gradient encoding can be repeated multiple times for additional GRE echoes. The full 3D trajectory is generated by rotating the 2D k-space trajectories.

### 4.2.2 Acquisition Method

For fMRI studies, we designed two protocols with different spatial and temporal resolution. We found that an odd number of RF pulses produced more uniform 2D k-space coverage in the highly undersampled fMRI cases, so we used 23 RF pulses with 1.12ms readout per RF pulse in mid-res protocol to achieve 3mm isotropic spatial resolution and 3.6s temporal resolution, and 31 RF pulses with 0.84ms readout per RF pulse for low resolution protocol to achieve 3.75mm isotropic spatial resolution and 1.8s temporal resolution. The RF pulse interval and gradient waveforms were adjusted such that the echo time is approximately 27.67ms for both protocols. To produce an excitation profile that is as uniform as possible, we used a series of very short 12$\mu$s RF pulses with near maximum magnitude in the excitation module with a flip angle of $3^\circ$.

For all protocols, we first designed a 2D sinusoidal gradient with acquisition dwell time of 4$\mu$s, a maximum gradient amplitude of 5 mT/m and maximum slew rate of 1 mT/m/ms in terms of the root sum of square of x and y axes. Then in 3D, to achieve more uniform k-space spokes, we adopted the 3D golden-angle based rotation [33] by generating a series of azimuth and polar angles with small increment. The 2D k-space trajectories were rotated along x axis by the azimuth angle and along the z axis by polar angle. We used 4800 3D rotations in hi-res protocol, 64 and 32 3D rotations for each time frame in mid-res and low-res fMRI protocols respectively. The structural and fMRI protocols are tested in phantom and in-vivo studies.

Because TOPPE v4 requires the gradient of each module to start and end at zero, we used ramp-up and ramp-down gradients before and after the excitation and acquisition module to accommodate this constraint. The max slew rate of the ramp up and ramp down gradient was set to 5 mT/m/ms.

Sensitivity maps were estimated from a 2 minute 3D GRE pulse sequence with Cartesian spin-wrap sampling with 3mm isotropic spatial resolution.

To test the performance of the proposed methods in the presence of different temporal coherence, we designed several temporal sampling patterns to evaluate how the undersampling effect might affect the reconstruction and temporal activities.

### 4.2.3 Model based reconstruction in looping-star

To effectively resolve the overlapping-echo artifacts, we used the model-based reconstruction for looping-star [27]. With the signal model and system matrix derived in [22], we use the conjugate gradient method to optimize the following cost function

$$\hat{\mathbf{X}} = \arg\min_{\mathbf{X}} \frac{1}{2}\|\mathcal{A}(\mathbf{X}) - \mathbf{y}\|_2^2 + \beta R(\mathbf{X}), \tag{4.1}$$

where $\mathbf{X} \in \mathbb{C}^{N_s \times N_t}$ is space-time image series to be reconstructed, $\mathcal{A}$ is the forward operator that maps the space-time image series to the vectorized k-space time series, and $R(\mathbf{X}) = \|\boldsymbol{T}\mathbf{X}\|_2^2$ is a 3D roughness regularizer using quadratic 1st-order finite differences with 26 neighbors. To get a reconstruction estimation $\hat{\mathbf{X}}$, one may use iterative reconstruction algorithms.

### 4.2.4 Spatial-Temporal reconstruction using UNFOLD in looping-star

"Unaliasing by Fourier-encoding the overlaps in the temporal dimension" (UNFOLD) [41] is a temporal strategy that involves changing the k-space sampling pattern from frame to frame, and applying temporal filters.

In this work, we combined two methods to reduce the undersampling artifact and improve the temporal resolution. First, we applied our previously described model-based reconstruction for overlapping echoes, which has less undersampling than the coherence resolved method [20]. Second, we used UNFOLD [41] to improve the temporal resolution by a factor of 2 and to reduce the undersampling artifact due to the alternating sampling patterns.

For the spatial-temporal reconstruction, we first split every frame into two sub-frames with equal duration and then separately reconstructed each sub-frame. Finally we applied UNFOLD along the temporal dimension to remove the undersampling artifact from the alternating sampling pattern. The UNFOLD filter can be chosen carefully to filter only a narrow frequency band (as shown in Fig. 4.2(a)) related to the undersampling pattern, while preserving the remainder of the temporal resolution.

#### 4.2.4.1 Problem formulation

In looping-star MRI, gradient echoes are overlapped in the time domain due to multiple RF pulses. Therefore, we use the signal model (3.7) to account for multiple echoes. This signal model fully models both echo-in and echo-out spokes and resolves the overlapping echo problems.

#### 4.2.4.2 Reconstruction

We used CG-SENSE with a spatial 3D quadratic roughness regularizer for reconstruction. Each frame from the scan is reconstructed independently using (3.8) as a reference. For the spatial-temporal reconstruction, we first split every frame into two sub-frames with equal duration and separately reconstructed each sub-frame. Then we used UNFOLD to remove the undersampling artifact from the alternating sampling pattern.

### 4.2.5 Spatial-Temporal reconstruction using LLR in looping star

#### 4.2.5.1 Global low-rank reconstruction

In MRI reconstruction, maintaining the integrity of the reconstructed image while promoting certain desirable properties, such as low-rank, is crucial. The global low-rank (GLR) model addresses this by introducing a regularization term that enforces a low-rank structure across the entire image matrix. The following cost function exemplifies the GLR approach:

$$f(\mathbf{X}) = \frac{1}{2}\|\mathcal{A}(\mathbf{X}) - \mathbf{y}\|_2^2 + \lambda\|\mathbf{X}\|_*, \tag{4.2}$$

where $\mathbf{X} \in \mathbb{C}^{N_s \times N_t}$ is space-time image series to be reconstructed, $\|\cdot\|_*$ represents the nuclear norm. This norm serves as a convex surrogate for the rank of $\mathbf{X}$, promoting a spectrum where few singular values are significant, thereby encouraging a low-rank structure of the entire image, $\lambda$ is a regularization parameter that balances the trade-off between data fidelity and the low-rank enforcement.

#### 4.2.5.2 Traditional locally low-rank reconstruction

The locally low-rank (LLR) model enhances MRI reconstruction by imposing a low-rank constraint on localized regions of the image, allowing for better preservation of local structures while reducing noise and artifacts. This model is particularly effective in capturing fine details and variations that might be lost under global regularization approaches. The LLR cost function is formulated as follows:

$$f(\mathbf{X}) = \frac{1}{2}\|\mathcal{A}(\mathbf{X}) - \mathbf{y}\|_2^2 + \lambda \sum_{p \in \text{patches}} \|\mathcal{P}_p(\mathbf{X})\|_*, \tag{4.3}$$

where $\mathcal{P}_p$ is an operator that extract patches from the 4D data to cover different local regions.

By applying the low-rank constraint locally, the LLR model adapts to the unique features of each region, thereby preserving details and structures that are vital for accurate temporal analysis. This technique is advantageous in dynamic and functional MRI, where it is crucial to maintain the integrity of temporal and functional variations.

#### 4.2.5.3 Proposed differentiable locally low-rank reconstruction

If the patches are non-overlapping, then the regularizer is "prox friendly" and we can apply proximal gradient methods like proximal optimized gradient method (POGM) [42, 43]. However, non-overlapping patches lead to block boundary artifacts. Using overlapping patches avoids those artifacts, but then the regularizer is not "prox friendly" and POGM is not applicable. There is an alternative regularizer that replaces the nuclear norm with the sum of a hyperbola function $\psi(\cdot)$ of the singular values. This function closely approximates the nuclear norm, but is differentiable, enabling gradient-based methods and providing the convergence guarantees. Inspired in part by the work [44], we investigated the following cost function for the spatial-temporal reconstruction

$$\begin{aligned} f(\mathbf{X}) = &\frac{1}{2}\|\mathcal{A}(\mathbf{X}) - \mathbf{y}\|_2^2 \\ &+ \lambda \sum_{s \in \text{shifts}} \sum_{p \in \text{patches}} \sum_{k \geq 1} \psi(\sigma_k(\mathcal{P}_p(\mathcal{P}_s(\mathbf{D}_H \mathbf{X})))) \\ &+ \lambda \sum_{s \in \text{shifts}} \sum_{p \in \text{patches}} \sum_{k \geq 1} \psi(\sigma_k(\mathcal{P}_p(\mathcal{P}_s(\mathbf{D}_V \mathbf{X})))) \end{aligned} \tag{4.4}$$

where $\psi$ is a convex function applied to the singular values of the matrix patches. $\sigma_k$ denotes the $k$th singular values derived from the singular value decomposition (SVD) of the localized image patches. $\mathcal{P}_s$ is the patch shifting operators. $\mathbf{D}_H$ and $\mathbf{D}_V$ are horizontal and vertical spatial finite differences operators, respectively, enhancing spatial smoothness and continuity across the image.

We use the conjugate gradient method to rapidly minimize this differentiable LLR (DLLR) cost function with overlapping patches. Our approach utilizes shifts and patches to apply the regularization locally but comprehensively across the image.

### 4.2.6 Experiments

For the spatial-temporal reconstruction, we compared our proposed methods with 1) lower temporal resolution, 2) higher temporal resolution before UNFOLD filtering, and 3) higher temporal resolution after UNFOLD filtering, 4) higher temporal resolution using DLLR reconstruction and UNFOLD filtering. In the fMRI study, participants watched a flashing

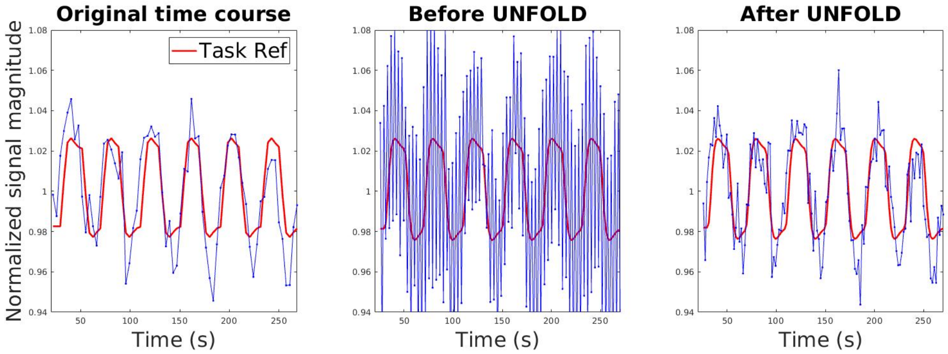

**FIG** 4.1 – fMRI time course from visual stimulus. Left to right: reconstruction with 3.6 sec temporal resolution; reconstruction with 1.8 sec temporal resolution without UNFOLD; reconstruction with 1.8sec temporal resolution with UNFOLD. Due to the high undersampling rate, the middle figure shows significant signal oscillation from the different sampling trajectories when we reduce the time for each frame. After removing the undersampling artifact in the k-t domain using UNFOLD, the oscillations are mostly removed and temporal resolution is also improved.

checkerboard for multiple cycles (20s on and 20s off), and were required to tap their fingers while the checkerboard was on. The pulse sequences were programmed via TOPPE [7]and implemented on a GE UHP 3.0T scanner with a Nova 32RX head coil. Subjects gave informed consent under IRB approval. For looping star protocols used in both UNFOLD and LLR, we set the volume TR to be 3.6s, number of sampled points per spoke to be 292, number of spoke per 2D plane to be 23, number of planes per volume to be 32, and the echo time to be 30.7msec.

## 4.3 Results

### 4.3.1 Looping-star reconstruction with UNFOLD

Figure 4.1 shows the time series of a looping-star fMRI task. It can be seen that the undersampling artifact in (b) due to the repeating sampling pattern is significantly reduced after applying UNFOLD (c), leading to increased temporal resolution and reduced undersampling artifact.

Figure 4.2: (a) shows the FFT of the time course of a typical activated voxel. There is a significant high-frequency component because the undersampling artifact oscillates between adjacent frames. Before UNFOLD, the raw activation map (b) does not reflect the

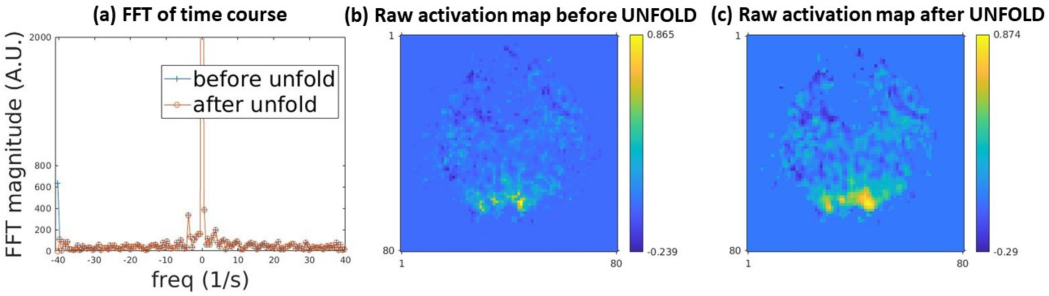
(a) FFT of time course (b) Raw activation map before UNFOLD (c) Raw activation map after UNFOLD

**FIG** 4.2 – shows the FFT of a time course of a typical activated voxel. Before UNFOLD, the raw activation map does not reflect the true brain activity because the undersampling artifacts oscillate between adjacent frames. After UNFOLD, even only removing a single frequency component, the undersampling artifact is reduced such that the new activation map shows higher correlation coefficient and recovered activities.

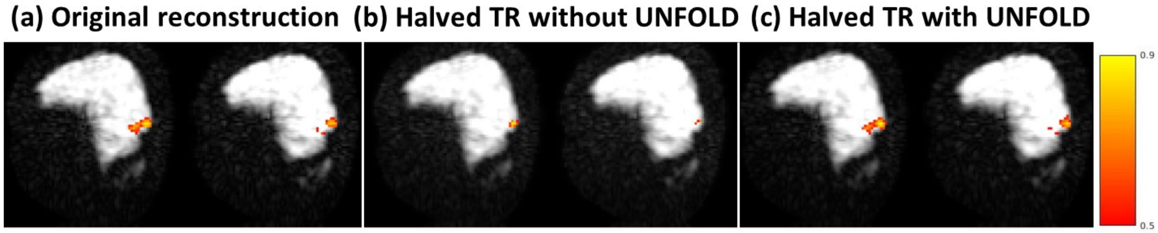
(a) Original reconstruction (b) Halved TR without UNFOLD (c) Halved TR with UNFOLD

**FIG** 4.3 – fMRI time course from visual stimulus. Left to right: reconstruction with 3.6 sec temporal resolution; reconstruction with 1.8 sec temporal resolution without UNFOLD; reconstruction with 1.8sec temporal resolution with UNFOLD. Due to the high undersampling rate, the middle figure shows significant signal oscillation from the different sampling trajectories when we reduce the time for each frame. After removing the undersampling artifact in the k-t domain using UNFOLD, the oscillations are mostly removed and temporal resolution is also improved.

true brain activity due to the undersampling artifacts. After UNFOLD, even by only removing a single frequency component, the new activation map (c) shows higher correlation coefficients and recovered activities.

Figure 4.3: Sagittal activation map for the visual stimulus. Improving the temporal resolution by a factor of 2 (from (a) to (b)) initially greatly reduces activation,due to the increased noise from the undersampling artifacts. However, after removing the undersampling artifact using UNFOLD, the activation map is improved back to the level of the original reconstruction, but with doubled temporal resolution.

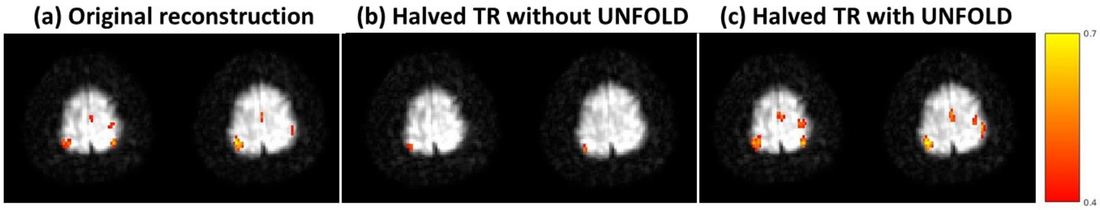

**FIG** 4.4 – shows the FFT of a time course of a typical activated voxel. Before UNFOLD, the raw activation map does not reflect the true brain activitybecause the undersampling artifacts oscillate between adjacent frames. After UNFOLD, even only removing a single frequency component, theundersampling artifact is reduced such that the new activation map shows higher correlation coefficient and recovered activities.

Figure 4.4 shows the activation map for the finger-tapping tasks. Similar to the visual task, using UNFOLD recovers brain activities by reducing the undersampling artifact.

### 4.3.2 Looping-star reconstruction using LLR

For a non-repeating pattern, we reconstruct a 20s golden-angle based sampling pattern with 2s temporal resolution, and compared the frame-wise reconstruction versus the DLLR reconstruction. the LLR method improved the image qualities and reduced the undersampling artifacts by utilizing the k-space information from different sampling pattern as shown in Figure 4.5.

For repeating sampling pattern, we first explored the possibility of just using UNFOLD approach, for which an alternating sampling pattern leads to an alternating undersampling artifact, which can be filtered out with negligible impact on the temporal resolution as shown in Figure 4.6. While the sampling pattern lacks the temporal incoherence we would consider optimal for LLR methods, we have applied a differentiable LLR reconstruction to UNFOLD data using $5 \times 5 \times 3 \times 10$ (x y z t) patches, leading to a 3.5 dB improvement in temporal SNR (tSNR), which measures the ratio of the mean signal to the standard deviation of the noise over time (see Figure 4.6).

## 4.4 Conclusion

This work has two purposes: 1) reducing spatial undersampling artifacts while maintaining the desired higher temporal resolution and 2) improving the tSNR by removing noise and artifact components. Our results demonstrated that a simple UNFOLD processing

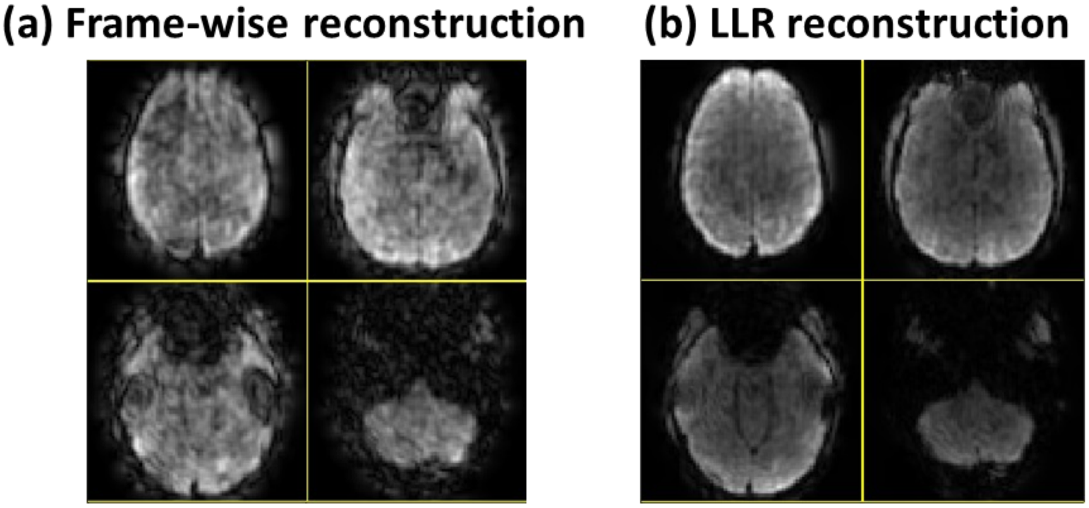

**FIG** 4.5 – Frame-wise and DLLR reconstruction. The DLLR significantly improved the image qualities and reduce the undersampling artifacts as compared to the frame-wise reconstruction.

approach can reduce undersampling artifacts and improve temporal resolution as demonstrated on both visual and motor tasks, but is best suited to dynamic k-space sampling that alternates between just two patterns. Later we investigated and compared a sophisticated 4D (3D space + time) image reconstruction methods DLLR for more general dynamic k-space sampling patterns. The basic idea is to exploit the the redundancy of stationary/low-rank components of the signal model. The DLLR reconstruction showed significantly improved image qualities and reduced undersampling artifacts when using non-repeating patterns, and improved activation map and tSNR compared to only UNFOLD methods when using sub-optimal repeating sampling patterns.

## 4.5 Future work

We hope to demonstrate functional analysis of the DLLR method with a suitable non-repearting sampling pattern. Also, the LLR and DLLR methods capture important low-rank properties in a manner that is data-driven for each individual subject, but do not capture potential dimensionality reduction opportunities that could be provided by sparsifying transforms that are refined in a data-driven way using data from multiple subjects. Recent work (for 2D static imaging) has demonstrated that sparsity-based reconstruction methods with as few as about 100 learnable parameters can perform nearly as well as deep networks when trained properly [45]. A future direction is to extend the DLLR approach

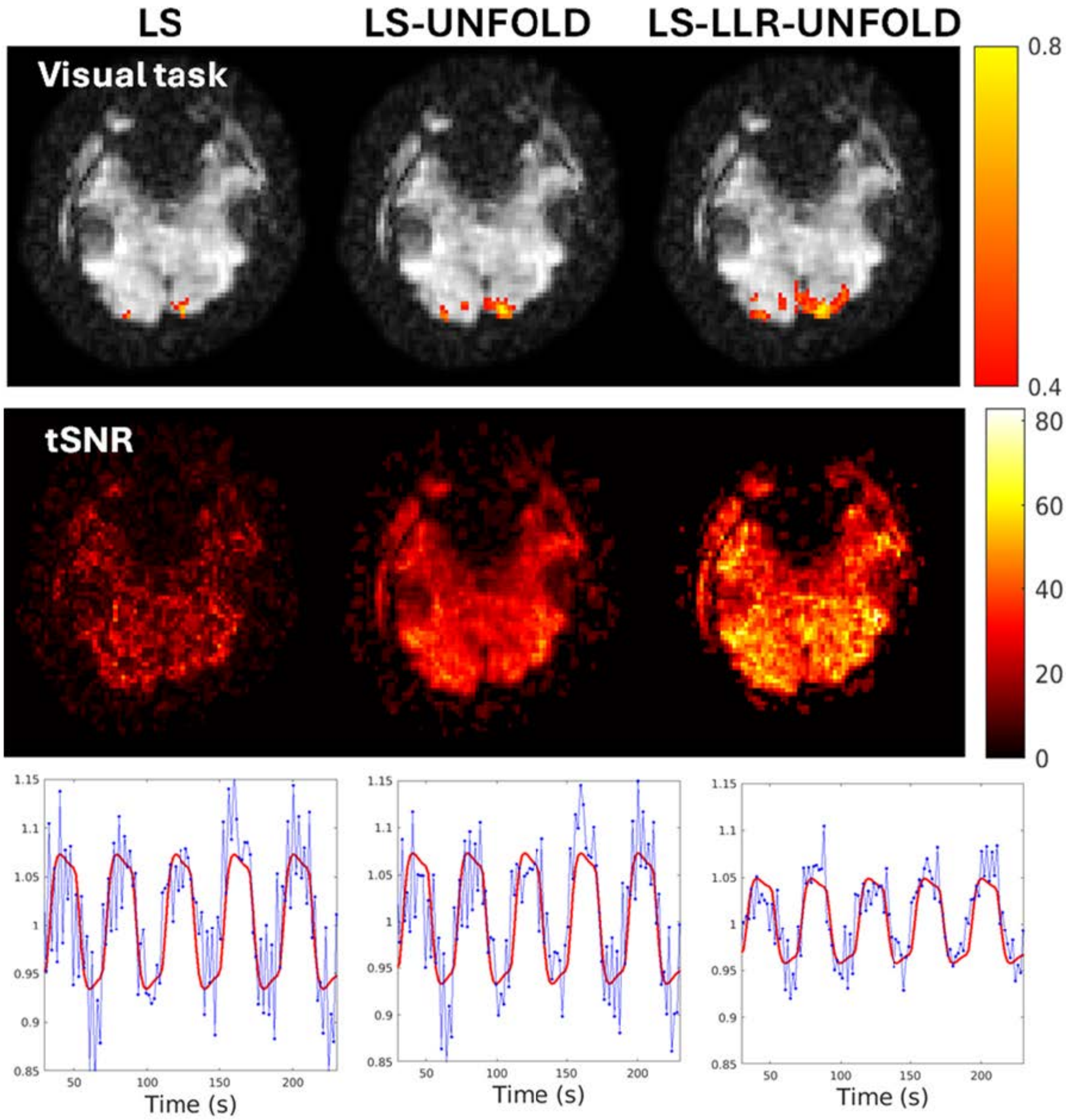

**FIG** 4.6 – Frame-wise, UNFOLD, and LLR-UNFOLD reconstruction (L to R). 1st row: activation maps in visual cortex, 2nd row: temporal SNR maps, 3rd row: activation time course. Use of the LLR reconstruction improved average tSNR by 3.5dB. The LLR recon did not improve the underlying image due to a sub-optimal sampling pattern.

to a DLLR + sparse (DLLR+S) regularizer using combinations of wavelet transforms (in time and space) and temporal Fourier transforms.

# CHAPTER 5

# Learning-based k-space Trajectory Optimization for Silent Looping-star

Magnetic Resonance Imaging (MRI) systems predominantly acquire data in the frequency domain (k-space) following specific sampling trajectories. Efficient sampling strategies are crucial for accelerating acquisition and enhancing image quality. This study concentrates on optimizing 3D non-Cartesian trajectories for looping star patterns utilizing a generalized gradient-based optimization approach for automatic trajectory design and tailoring. Traditionally, the design of sampling patterns in MRI considers properties of k-space signals, with variable density (VD) trajectories being a common choice for 2D sampling. However, designing 3D sampling patterns poses additional challenges due to increased parameter complexity, the necessity to account for advanced reconstruction methods, and the potential for peripheral nerve stimulation (PNS) effects. To address these challenges, we propose a learning-based method to jointly optimize reconstruction and sampling patterns. Our approach involves two parameterizations: (1) using fixed 2D trajectories and optimizing their scaling factor and rotation angles, and (2) employing a novel parameterization to directly design the 3D gradient waveforms through the superposition of sinusoidal harmonics to meet re-focusing gradient requirements. We evaluated the optimized trajectories on a physical phantom and in-vivo fMRI data, observing improved point spread function (PSF) characteristics, reduced noise, and diminished undersampling artifacts compared to traditional trajectories using random or golden-angle-based rotations.

## 5.1 Introduction

Most MRI systems sample data in the frequency domain (k-space) following prescribed sampling trajectories. Efficient sampling strategies can accelerate acquisition and improve

---

This chapter is recent work in collaboration with Dr. Guanhua Wang, to be submitted for publication..

image quality. Many well-designed sampling strategies and their variants, such as spiral, radial, CAIPIRINHA, and PROPELLER [46, 47, 48, 49] have enabled MRI's application to many areas. Sampling patterns in k-space either are located on the Cartesian raster or arbitrary locations (non-Cartesian sampling). This work focuses on optimizing 3D non-Cartesian trajectories for looping star using a generalized gradient-based optimization method for automatic trajectory design/tailoring.

The design of sampling patterns usually considers certain properties of k-space signals. For instance, the variable density (VD) spiral trajectory samples more densely in the central k-space where more energy is located. For higher spatial frequency regions, the VD spiral trajectory uses larger gradient strengths and slew rates to cover as much of k-space as quickly as possible. Compared to 2D sampling, designing 3D sampling by hand is more challenging for several reasons. The number of parameters increases in 3D, and thus the parameter selection is more difficult due to the larger search space. Additionally, analytical designs usually are based on the Shannon-Nyquist relationship that might not fully consider properties of sensitivity maps and advanced reconstruction methods. For 3D sampling pattern with a high undersampling (acceleration) ratio, there are limited analytical tools for designing sampling patterns having anisotropic FOV and resolution. For these reasons, it is important to automate the design of 3D sampling trajectories.

A learning-based method was proposed to jointly optimize the reconstruction and sampling pattern [36]. In that work, k-space sampling trajectories can be parameterized by some differentiable basis functions and then be optimized through the gradient-based method. To apply this sampling optimization in looping star, we proposed to 1) use fixed 2D trajectories and then optimize the 3D rotation angles; 2) optimize the magnitude and phase of the sinusoidal gradient; 3) employ a novel parameterization to directly design the 3D gradient waveforms using the superposition of sinusoidal harmonics to meet refocusing gradient requirements.

We optimized the trajectories using the parameterizations mentioned above and tested them on a physical phantom. The point spread function (PSF) of the optimized trajectories exhibited more centered energy around the k-space origin, and fewer streaking artifacts were observed. The reconstructed images showed reduced noise and undersampling artifacts compared to previous trajectories.

We tested the optimized trajectories on in-vivo fMRI data and compared them to previous classic trajectories that used random or golden-angle based rotations. The reconstructed images showed improved spatial resolution and reduced noises due to the more uniform distributed sampling patterns.

## 5.2 Methods

### 5.2.1 Trajectories initialization

We used both random rotations and golden angle based rotations to initialize the trajectories and then optimize the gradients and trajectories over either initialization.

Random rotations was used in the looping-star low spatial resolution protocol for the fMRI tasks. Here we use 31 RF pulses with 0.84ms readout per RF pulse to achieve about 3 mm isotropic resolution and 1.86s temporal resolution, which we call the low-resolution protocol. Only one GRE echo is collected to acquire images with TE $= 27.67$ms.

For fMRI studies, we designed two protocols with different spatial and temporal resolution. We found that an odd number of RF pulses produced more uniform 2D k-space coverage in the highly undersampled fMRI cases, The RF pulse interval and gradient waveforms were adjusted such that the echo time is approximately 27.67ms for both protocols. To produce an excitation profile that is as uniform as possible, we used a series of very short 12$\mu$s RF pulses with near maximum magnitude in the excitation module with a flip angle of 3$^\circ$.

The generalized golden-angle based rotations improves the uniformity in terms of the k-space samples, leading to reduced undersampling artifacts and improved image qualities. So we used 23 RF pulses with 1.12ms readout per RF pulse in mid-res protocol to achieve 3mm isotropic spatial resolution and 3.6s temporal resolution.

### 5.2.2 Gradient parameterization

Instead of designing 2D gradient waveform and then applying rotations, we directly optimized the 3D gradient waveforms. The gradient waveforms using sinusoidal harmonics can be expressed as

$$g_x(t) = \sum_{i=1}^{N} c_{x,i} \sin\left(\frac{2\pi t \cdot i}{T_\mathrm{E}} + \theta_{x,i}\right) \tag{5.1}$$

$$g_y(t) = \sum_{i=1}^{N} c_{y,i} \sin\left(\frac{2\pi t \cdot i}{T_\mathrm{E}} + \theta_{y,i}\right) \tag{5.2}$$

$$g_z(t) = \sum_{i=1}^{N} c_{z,i} \sin\left(\frac{2\pi t \cdot i}{T_\mathrm{E}} + \theta_{z,i}\right), \tag{5.3}$$

where $g_x(t), g_y(t), g_z(t)$ are the 3D gradient waveforms, $c_{x,i}$ and $\theta_{x,i}$ are the coefficients that control the magnitude and phase of the $i$th order harmonic respectively, and $N$ is the number determining the highest order of the harmonics. By using this parameterization, previously hand-crafted sinusoidal gradient waveforms naturally fall within the span of our parameterization. To approximate piecewise linear gradient waveforms, one can solve a least squares problem to find the best approximation using our parameterization.

### 5.2.3 Reconstruction

With the system matrix derived in [22], we use the conjugate gradient method for frame by frame image reconstruction by optimizing the following cost function

$$\hat{\boldsymbol{x}} = \arg\min_{\boldsymbol{x}} \|\boldsymbol{s} - \boldsymbol{A}(\omega)\boldsymbol{C}\boldsymbol{x}\|_2^2 + \beta R(\boldsymbol{x}), \tag{5.4}$$

where $\boldsymbol{A}$ is the system matrix accounting for the overlapping echoes with given trajectories $\omega$ and $R(\boldsymbol{x}) = \|\boldsymbol{T}\boldsymbol{x}\|_2^2$ is a 3D roughness regularizer using quadratic 1st-order finite differences with 26 neighbors.

To get a reconstruction estimation $\hat{\boldsymbol{x}}$, one may use iterative reconstruction algorithms. Specifically, the algorithm should be step-wise differentiable (or sub-differentiable) to enable differentiable programming. The back propagation uses the chain rule to traverse every step of the iterative algorithm to calculate gradients with respect to variables such as $\omega$.

## 5.3 Jacobian Expressions

This section used the key Jacobian expressions and their efficient approximations based on NUFFT operations derive in [50]. These approximations enable the applications that follow.

### 5.3.1 Lemmas

We denote matrices, vectors and scalars by $\boldsymbol{A}$, $\boldsymbol{a}$ and $a$, respectively. $\boldsymbol{A}'$, $\boldsymbol{A}^T$ and $\boldsymbol{A}^*$ denote the Hermitian transpose, the transpose and the complex conjugate of $\boldsymbol{A}$, respectively.

Consider a scalar function $f(z),\ z = x + y\imath \in \mathbb{C},\ x, y \in \mathbb{R}$. Following the conventions in Wirtinger calculus [51, p. 67], the differential operators are defined as

$$\frac{\partial}{\partial z} = \frac{1}{2}\frac{\partial}{\partial x} - \frac{\imath}{2}\frac{\partial}{\partial y},\ \frac{\partial}{\partial z^*} = \frac{1}{2}\frac{\partial}{\partial x} + \frac{\imath}{2}\frac{\partial}{\partial y}.$$

A function $f$ is *complex differentiable* or *holomorphic* iff $\frac{\partial f}{\partial z^*} = 0$ (Cauchy–Riemann equation) [51, p. 66]. In the context of optimization, a cost function $L$ (usually a real scalar) is not holomorphic w.r.t. complex variables. A common approach (as adopted by PyTorch and TensorFlow) regards the real and imaginary components of a complex variable as two real-valued variables, and updates them separately, similar to the real-valued calculus [52]. For example, the $n$th gradient descent step uses the update

$$\boldsymbol{z}_{n+1} = \boldsymbol{z}_n - \alpha \left( \frac{\partial L}{\partial \boldsymbol{x}} + \imath \frac{\partial L}{\partial \boldsymbol{y}} \right) = \boldsymbol{z}_n - 2\alpha \frac{\partial L}{\partial \boldsymbol{z}^*},$$

where $\alpha \in \mathbb{R}^+$ denotes the step size. The chain rule still applies to calculating $\frac{\partial L}{\partial \boldsymbol{z}^*}$ [53] [51, p. 68]; for $s = f(z)$:

$$\frac{\partial L}{\partial \boldsymbol{z}^*} = \left( \frac{\partial L}{\partial \boldsymbol{s}^*} \right)^* \frac{\partial \boldsymbol{s}}{\partial \boldsymbol{z}^*} + \frac{\partial L}{\partial \boldsymbol{s}^*} \left( \frac{\partial \boldsymbol{s}}{\partial \boldsymbol{z}} \right)^* . \tag{5.5}$$

For Jacobian matrices, we follow the "numerator-layout" notation [54]. For example, the derivative of an $m$-element column vector $\boldsymbol{y}$ w.r.t. an $n$-element vector $\boldsymbol{x}$ is an $m \times n$ matrix:

$$\frac{\partial \boldsymbol{y}}{\partial \boldsymbol{x}} \triangleq \begin{bmatrix} \frac{\partial y_1}{\partial x_1} & \frac{\partial y_1}{\partial x_2} & \cdots & \frac{\partial y_1}{\partial x_n} \\ \frac{\partial y_2}{\partial x_1} & \frac{\partial y_2}{\partial x_2} & \cdots & \frac{\partial y_2}{\partial x_n} \\ \vdots & \vdots & \ddots & \vdots \\ \frac{\partial y_m}{\partial x_1} & \frac{\partial y_m}{\partial x_2} & \cdots & \frac{\partial y_m}{\partial x_n} \end{bmatrix} . \tag{5.6}$$

However, this convention does not handle scenarios such as the derivatives of the elements of one matrix w.r.t. the elements of another matrix. Thus, we adopt a natural extension by using the $\operatorname{vec}$ (vectorization) operation. Specifically, for a $M \times N$ matrix $\boldsymbol{A}$ that is a function of a $P \times Q$ matrix $\boldsymbol{B}$, we write the derivative as a $MN \times PQ$ matrix by applying (5.6) to the $\operatorname{vec}$ of each matrix:

$$\mathcal{D}_{\boldsymbol{B}}\, \boldsymbol{A} = \mathcal{D}_{\boldsymbol{B}}\, \boldsymbol{A}(\boldsymbol{B}) \triangleq \frac{\partial \operatorname{vec}(\boldsymbol{A})}{\partial \operatorname{vec}(\boldsymbol{B})}. \tag{5.7}$$

The following equalities are useful in our derivations. (Equalities involving products all assume the sizes are compatible.) For $\boldsymbol{A} \in \mathbb{C}^{K \times L},\ \boldsymbol{B} \in \mathbb{C}^{L \times M},\ \boldsymbol{C} \in \mathbb{C}^{M \times N}$:

$$\begin{aligned} \operatorname{vec}(\boldsymbol{ABC}) &= (\boldsymbol{I}_N \otimes \boldsymbol{AB}) \operatorname{vec}(\boldsymbol{C}) \\ &= (\boldsymbol{C}^T \boldsymbol{B}^T \otimes \boldsymbol{I}_K) \operatorname{vec}(\boldsymbol{A}). \end{aligned} \tag{P1}$$

In general:

$$(\boldsymbol{A} \otimes \boldsymbol{B})(\boldsymbol{C} \otimes \boldsymbol{D}) = (\boldsymbol{A}\boldsymbol{C}) \otimes (\boldsymbol{B}\boldsymbol{D}). \tag{P2}$$

For $\boldsymbol{A} \in \mathbb{C}^{K \times L},\ \boldsymbol{B} \in \mathbb{C}^{M \times N}$:

$$\boldsymbol{A} \otimes \boldsymbol{B} = (\boldsymbol{I}_K \otimes \boldsymbol{B})(\boldsymbol{A} \otimes \boldsymbol{I}_N) = (\boldsymbol{A} \otimes \boldsymbol{I}_M)(\boldsymbol{I}_L \otimes \boldsymbol{B}). \tag{P3}$$

For $\boldsymbol{A} \in \mathbb{C}^{M \times N},\ \boldsymbol{x} \in \mathbb{C}^{N}$:

$$\mathcal{D}_{\boldsymbol{A}} (\boldsymbol{A}\boldsymbol{x}) = \boldsymbol{x}^T \otimes \boldsymbol{I}_M,\ \mathcal{D}_{\boldsymbol{A}^*} (\boldsymbol{A}\boldsymbol{x}) = \boldsymbol{0}. \tag{P4}$$

For an invertible matrix $\boldsymbol{A}$:

$$\begin{aligned} \boldsymbol{A} \in \mathbb{C}^{N \times N} \implies \mathcal{D}_{\boldsymbol{A}}\, \boldsymbol{A}^{-1} &= -(\boldsymbol{A}^T)^{-1} \otimes \boldsymbol{A}^{-1}, \\ \mathcal{D}_{\boldsymbol{A}^*}\, \boldsymbol{A}^{-1} &= \boldsymbol{0}. \end{aligned} \tag{P5}$$

The chain rule still holds for the extended Jacobian formulation. Suppose $F : \mathbb{C}^{K \times L} \to \mathbb{C}^{M \times N}$ and $G : \mathbb{C}^{M \times N} \to \mathbb{C}^{P \times Q}$ are both holomorphic. For $\boldsymbol{X} \in \mathbb{C}^{K \times L}$, the Jacobian of the composite function is:

$$\begin{aligned} &\underbrace{\mathcal{D}_{\boldsymbol{X}}\, G(F(\boldsymbol{X}))}_{PQ \times KL} = \underbrace{\mathcal{D}_{\boldsymbol{Y}}\, G(\boldsymbol{Y})|_{\boldsymbol{Y}=F(\boldsymbol{X})}}_{PQ \times MN}\, \underbrace{\mathcal{D}_{\boldsymbol{X}}\, F(\boldsymbol{X})}_{MN \times KL}, \\ &\mathcal{D}_{\boldsymbol{X}^*}\, G(F(\boldsymbol{X})) = \boldsymbol{0}. \end{aligned} \tag{P6}$$

Equalities (P1)-(P3) are common matrix vectorization properties. See [55, Ch. 9] for (P4), [53] for (P5) and (P6).

### 5.3.2 System Model

Consider the (single-coil, initially) MRI measurement model for non-Cartesian sampling based on the NUDFT [56]:

$$\boldsymbol{y} = \boldsymbol{A}\boldsymbol{x} + \boldsymbol{\varepsilon},$$

where $\boldsymbol{y} \in \mathbb{C}^M$ denotes the measured k-space data, $\boldsymbol{x} \in \mathbb{C}^N$ denotes the unknown image to be reconstructed, and $\boldsymbol{A} \in \mathbb{C}^{M \times N}$ denotes the system matrix or encoding matrix, where $\boldsymbol{A} = \boldsymbol{A}(\omega)$ has elements

$$a_{ij} = \mathrm{e}^{-\imath \vec{\omega}_i \cdot \vec{r}_j}, \quad i = 1, \ldots, M, \quad j = 1, \ldots, N \tag{5.8}$$

for $\vec{\omega}_i \in \mathbb{R}^D$ and $\vec{r}_j \in \mathbb{R}^D$ where $D \in \{1, 2, 3 \ldots\}$ denotes the image dimension, and where

$$\omega = [\omega^{[1]}\, \omega^{[2]} \ldots \omega^{[D]}]$$

is the $M \times d$ matrix consisting of all the k-space sampling locations and $\omega^{[d]} \in \mathbb{R}^M$ denotes its $d$th column. (For simplicity here, we ignore other physical effects like field inhomogeneity and relaxation that are sometimes included in the forward model in MRI [56].) The center locations of voxels $\{\vec{r}_j\}$ usually lie on a Cartesian grid, but the k-space sample locations $\omega$ in principle can be arbitrary subject to the Nyquist constraint.

Specifically, for looping star, two echos are recorded simultaneously, with corresponding trajectories denoted by $\omega_1$ and $\omega_2$. The system matrix is $\boldsymbol{A} = \boldsymbol{A}(\omega_1) + \boldsymbol{A}(\omega_2)$. Denote $\boldsymbol{A}_1 = \boldsymbol{A}(\omega_1)$ and $\boldsymbol{A}_2 = \boldsymbol{A}(\omega_2)$.

### 5.3.3 Forward Operator

We first focus on the forward operation. Following [50, (5)] the partial derivatives of $\boldsymbol{A}\boldsymbol{x}$ w.r.t. $\omega_1^{[d]}$ (an $M \times M$ Jacobian matrix) is:

$$\begin{aligned} \frac{\partial \boldsymbol{A}\boldsymbol{x}}{\partial \omega_1^{[d]}} &= \frac{\partial \boldsymbol{A}_1\boldsymbol{x} + \partial \boldsymbol{A}_2\boldsymbol{x}}{\partial \omega_1^{[d]}} = \frac{\partial \boldsymbol{A}_1\boldsymbol{x}}{\partial \omega_1^{[d]}} \\ &= -\imath \operatorname{Diag}\left\{\boldsymbol{A}_1(\boldsymbol{x} \odot \boldsymbol{r}^{[d]})\right\}. \end{aligned} \tag{5.9}$$

Similarly,

$$\frac{\partial \boldsymbol{A}\boldsymbol{x}}{\partial \omega_2^{[d]}} = -\imath \operatorname{Diag}\left\{\boldsymbol{A}_2(\boldsymbol{x} \odot \boldsymbol{r}^{[d]})\right\}. \tag{5.10}$$

Consequently, the Jacobian calculation should apply $\boldsymbol{A}$ to vector $\boldsymbol{x} \odot \boldsymbol{r}^{[d]}$ once. In the above derivation, $\boldsymbol{A}$ is a NUDFT operator. In the practical implementation, we use a NUFFT to approximate $\boldsymbol{A}$, both for the forward model and for the Jacobian calculation.

### 5.3.4 Adjoint Operator

The Jacobian matrix for adjoint-vector product is (following [50, (6)])

$$\frac{\partial \boldsymbol{A}'\boldsymbol{y}}{\partial \omega_1^{[d]}} = \imath \operatorname{Diag}\left\{\boldsymbol{r}^{[d]}\right\} \boldsymbol{A}_1' \operatorname{Diag}\{\boldsymbol{y}\}. \tag{5.11}$$

$$\frac{\partial \boldsymbol{A}'\boldsymbol{y}}{\partial \omega_2^{[d]}} = \imath \operatorname{Diag}\left\{\boldsymbol{r}^{[d]}\right\} \boldsymbol{A}_2' \operatorname{Diag}\{\boldsymbol{y}\}. \tag{5.12}$$

### 5.3.5 Gram Matrix

Here we derived the gram matrix for the looping-star sequence with two system matrices. Following [50, (10, 11)],

$$\begin{aligned}
&\mathcal{D}_{\omega_1^{[d]}} \boldsymbol{A}'\boldsymbol{A}\boldsymbol{x} \\
&= \mathcal{D}_{\omega_1^{[d]}} (\boldsymbol{A}_1 + \boldsymbol{A}_2)'(\boldsymbol{A}_1 + \boldsymbol{A}_2)\boldsymbol{x} \\
&= \mathcal{D}_{\omega_1^{[d]}} \boldsymbol{A}_1'\boldsymbol{A}_1\boldsymbol{x} + \mathcal{D}_{\omega_1^{[d]}} \boldsymbol{A}_1'\boldsymbol{A}_2\boldsymbol{x} + \mathcal{D}_{\omega_1^{[d]}} \boldsymbol{A}_2'\boldsymbol{A}_1\boldsymbol{x} \\
&= -\imath\, \boldsymbol{A}_1'\mathrm{Diag}\big\{\boldsymbol{A}_1(\boldsymbol{x} \odot \boldsymbol{r}^{[d]})\big\} \\
&\quad + \imath\, \mathrm{Diag}\big\{\boldsymbol{r}^{[d]}\big\}\, \boldsymbol{A}_1'\mathrm{Diag}\{\boldsymbol{A}_1\boldsymbol{x}\} \\
&\quad + \imath\, \mathrm{Diag}\big\{\boldsymbol{r}^{[d]}\big\}\, \boldsymbol{A}_1'\mathrm{Diag}\{\boldsymbol{A}_2\boldsymbol{x}\} \\
&\quad + \boldsymbol{A}_2'(-\imath\, \mathrm{Diag}\big\{\boldsymbol{A}_1(\boldsymbol{x} \odot \boldsymbol{r}^{[d]})\big\}) && (5.13) \\
&= -\imath \boldsymbol{A}'\mathrm{Diag}\big\{\boldsymbol{A}_1(\boldsymbol{x} \odot \boldsymbol{r}^{[d]})\big\} && (5.14) \\
&\qquad + \imath\, \mathrm{Diag}\big\{\boldsymbol{r}^{[d]}\big\}\, \boldsymbol{A}_1'\mathrm{Diag}\{\boldsymbol{A}\boldsymbol{x}\}
\end{aligned}$$

Similarly,

$$\begin{aligned}
&\mathcal{D}_{\omega_2^{[d]}} \boldsymbol{A}'\boldsymbol{A}\boldsymbol{x} \\
&= -\imath \boldsymbol{A}'\mathrm{Diag}\big\{\boldsymbol{A}_2(\boldsymbol{x} \odot \boldsymbol{r}^{[d]})\big\} && (5.15) \\
&\qquad + \imath\, \mathrm{Diag}\big\{\boldsymbol{r}^{[d]}\big\}\, \boldsymbol{A}_2'\mathrm{Diag}\{\boldsymbol{A}\boldsymbol{x}\}
\end{aligned}$$

### 5.3.6 Inverse of Positive Semidefinite (PSD) Matrix

Image reconstruction methods based on algorithms like the augmented Lagrangian approach [57] use “data consistency” steps [58, 59, 60] that often involve least-squares problems with solutions in the following form:

$$(\boldsymbol{A}'\boldsymbol{A} + \lambda \boldsymbol{I})^{-1}\boldsymbol{x},$$

for some vector $\boldsymbol{x} \in \boldsymbol{C}^N$, or

$$(\boldsymbol{A}'\boldsymbol{A} + \lambda \boldsymbol{T}'\boldsymbol{T})^{-1}\boldsymbol{x}, \tag{5.16}$$

where $\boldsymbol{T}$ denotes a linear regularization operator that is independent of $\omega$. In both cases, $\lambda > 0$ and the null spaces of $\boldsymbol{T}$ and $\boldsymbol{A}$ are disjoint, so the Hessian matrix is invertible. A few iterations of a CG method usually suffices to efficiently compute the approximate product of such a matrix inverse with a vector. The direct inverse is impractical for large-scale problems like MRI. Following [58], we treat CG as solving the above equations accurately, so that we can derive efficient approximations as follows. Otherwise, attempting to auto-differentiate through a finite number of CG iterations would require large amounts of memory. Here we derive the corresponding Jacobian matrices for the exact inverse to (5.16) and then apply fast approximations. For $\boldsymbol{x}$, the $N \times N$ Jacobian is

$$\begin{aligned} \frac{\partial (\boldsymbol{A}'\boldsymbol{A} + \lambda \boldsymbol{T}'\boldsymbol{T})^{-1}\boldsymbol{x}}{\partial \boldsymbol{x}} &= (\boldsymbol{A}'\boldsymbol{A} + \lambda \boldsymbol{T}'\boldsymbol{T})^{-1}, \\ \frac{\partial (\boldsymbol{A}'\boldsymbol{A} + \lambda \boldsymbol{T}'\boldsymbol{T})^{-1}\boldsymbol{x}}{\partial \boldsymbol{x}^*} &= 0. \end{aligned}$$

We can still use CG (with NUFFT) to efficiently multiply this Jacobian by a vector, albeit approximately.

To consider the Jacobian w.r.t. the sampling pattern $\omega^{[d]}$, define $\boldsymbol{z} = (\boldsymbol{A}'\boldsymbol{A}+\lambda \boldsymbol{T}'\boldsymbol{T})^{-1}\boldsymbol{x}$ and $\boldsymbol{F} = \boldsymbol{A}'\boldsymbol{A} + \lambda \boldsymbol{T}'\boldsymbol{T}$. Note that $\boldsymbol{A}$ now has two components from echo-in and echo-out spokes respectively. We assume that $\boldsymbol{A}$ and $\boldsymbol{T}$ have disjoint null spaces, so that $\boldsymbol{F}$ is positive definite and hence invertible. Applying equalities derived above leads to the following expression for the $M \times N$ Jacobian by using [50, (13)] and (5.13):

$$\begin{aligned} & \mathcal{D}_{\omega_1^{[d]}} \boldsymbol{F}^{-1}\boldsymbol{x} \\ & = -\boldsymbol{F}^{-1} \left( \mathcal{D}_{\omega_1^{[d]}} \boldsymbol{F}\boldsymbol{z} \right) \\ & = -(\boldsymbol{A}'\boldsymbol{A} + \lambda \boldsymbol{T}'\boldsymbol{T})^{-1} \Big( -\imath\, \boldsymbol{A}_1' \mathrm{Diag}\big\{ \boldsymbol{A}_1 (\boldsymbol{z} \odot \boldsymbol{r}^{[d]}) \big\} \\ & \qquad + \imath\, \mathrm{Diag}\big\{ \boldsymbol{r}^{[d]} \big\}\, \boldsymbol{A}_1' \mathrm{Diag}\{ \boldsymbol{A}_1 \boldsymbol{z} \} \\ & \qquad + \imath\, \mathrm{Diag}\big\{ \boldsymbol{r}^{[d]} \big\}\, \boldsymbol{A}_1' \mathrm{Diag}\{ \boldsymbol{A}_2 \boldsymbol{z} \} \\ & \qquad + \boldsymbol{A}_2' (-\imath\, \mathrm{Diag}\big\{ \boldsymbol{A}_1 (\boldsymbol{z} \odot \boldsymbol{r}^{[d]}) \big\}) \Big) \end{aligned} \tag{5.17}$$

$$\begin{aligned}
&\mathcal{D}_{\omega_2^{[d]}} \boldsymbol{F}^{-1}\boldsymbol{x} \\
&= -\boldsymbol{F}^{-1}\left(\mathcal{D}_{\omega_2^{[d]}} \boldsymbol{F}\boldsymbol{z}\right) \\
&= -(\boldsymbol{A}'\boldsymbol{A} + \lambda \boldsymbol{T}'\boldsymbol{T})^{-1}\Big( -\imath\, \boldsymbol{A}_2' \mathrm{Diag}\big\{\boldsymbol{A}_2(\boldsymbol{z} \odot \boldsymbol{r}^{[d]})\big\} \\
&\qquad\qquad + \imath\, \mathrm{Diag}\big\{\boldsymbol{r}^{[d]}\big\}\, \boldsymbol{A}_2' \mathrm{Diag}\{\boldsymbol{A}_2 \boldsymbol{z}\} \\
&\qquad\qquad + \imath\, \mathrm{Diag}\big\{\boldsymbol{r}^{[d]}\big\}\, \boldsymbol{A}_2' \mathrm{Diag}\{\boldsymbol{A}_1 \boldsymbol{z}\} \\
&\qquad\qquad + \boldsymbol{A}_1'(-\imath\, \mathrm{Diag}\big\{\boldsymbol{A}_2(\boldsymbol{z} \odot \boldsymbol{r}^{[d]})\big\})\Big) \qquad (5.18)
\end{aligned}$$

We apply this Jacobian to a vector by using four NUFFT operations followed by running CG to approximate the product of $\boldsymbol{F}^{-1}$ times a vector.

## 5.4 Experiments

The proposed method reduced the undersampling artifacts in both low-resolution and mid-resolution over either random or golden angle based rotations.

### 5.4.1 Optimized trajectories

To balance the trade off between the computational cost and number of parameters to optimize, we tried different number of $N$ and empirically found $N = 5$ in (5.3) could introduce enough higher-order harmonics and bend the k-space trajectories to the k-space corners. The magnitude of higher-order harmonics is small and the acoustic noise level using the optimized trajectories remains similar to previous looping-star pulse sequences.

Figure 5.1 shows the trajectories using random rotations, generalized golden-angle rotations, trajectory from optimized magnitude and phase, and trajectory from optimized parameterized gradients. It can be observed that the optimized trajectories reach out further to the k-space corner, therefore potentially improving the spatial resolution.

### 5.4.2 Point Spread Function

We compared the Point Spread Function (PSF) of the trajectories before and after the optimization. The trajectory is initialized with random rotation, leading to non-uniform PSF and streaking artifacts as shown in figure 5.2. Figure 5.2 also shows that the optimized

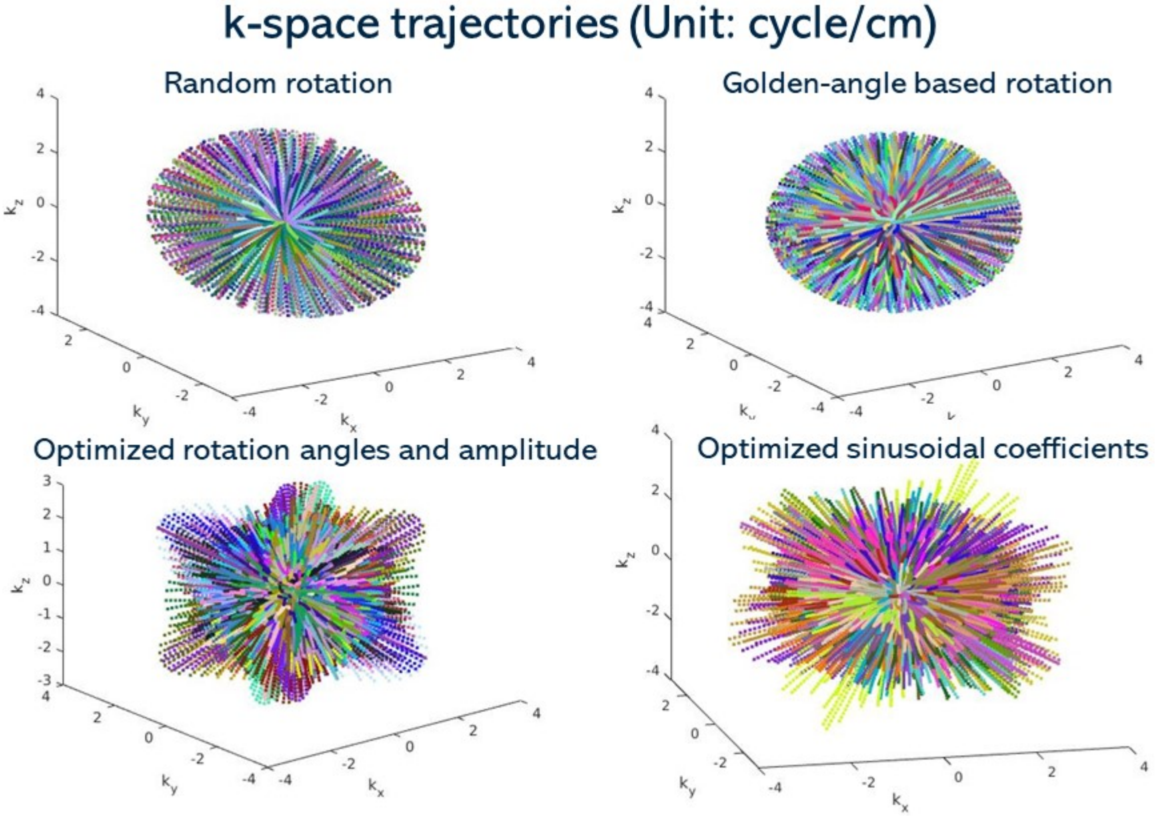

**FIG** 5.1 – Trajectories using random rotations, generalized golden-angle rotations, trajectory from optimized magnitude and phase, and trajectory from optimized parameterized gradients. It can be observed that the Optimized trajectories reach out further to the k-space corner, therefore capable of improving the spatial resolution.

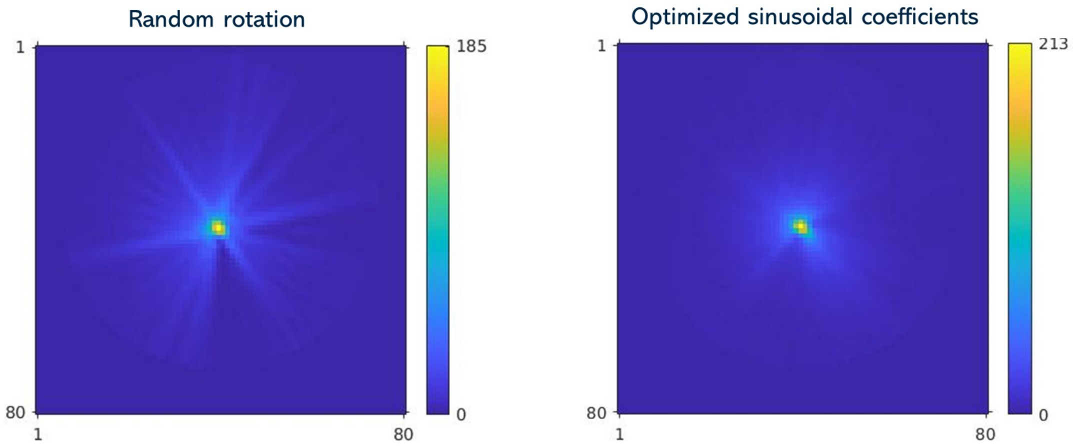

**FIG** 5.2 – PSF of trajectories with random rotation and optimized sinusoidal coefficients. The optimized trajectory has reduced streaking artifacts and also more centered energy, which implies potential improved resolution and sharpness.

trajectory has reduced streaking artifacts and also more centered energy, which implies potential improved resolution and sharpness.

### 5.4.3 Phantom Study

Figure 5.3 shows the reconstructions of a structured phantom using the low-resolution protocol (3.75mm isotropic) with random rotations and optimized trajectory (20X undersampled). We used a 20X undersampling factor due to the memory limitations on gradient waveforms present in the GE scanner during our sequence implementation. It can be observed that the reconstruction of optimized trajectory led to higher spatial resolution and less image noise as compared to the reconstruction of random rotations. Note that the phantom is out-of-distribution, as the trajectory was trained on the T1-weighted Calgary dataset.

### 5.4.4 In-vivo study

Figure 5.4 shows the reconstructions of a human brain using the low-resolution protocol (3.75mm isotropic) with random rotations and optimized trajectory. It can be seen that the optimized trajectories lead to more recovered structure.

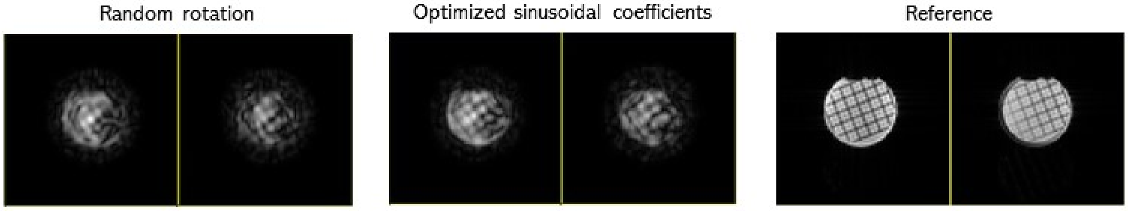

**FIG** 5.3 – Reconstructions of a structured phantom using the low-resolution protocol (3.75 mm isotropic) with random rotations and optimized trajectory (2 consecutive slices). The reference image was acquired from a GRE separate scan with approximately zero echo time. Although it is not perfectly registered to the looping-star image, it is displayed to illustrate the phantom's structure. The reconstruction using the optimized trajectory demonstrated better spatial resolution and reduced image noise compared to the reconstruction using random rotations.

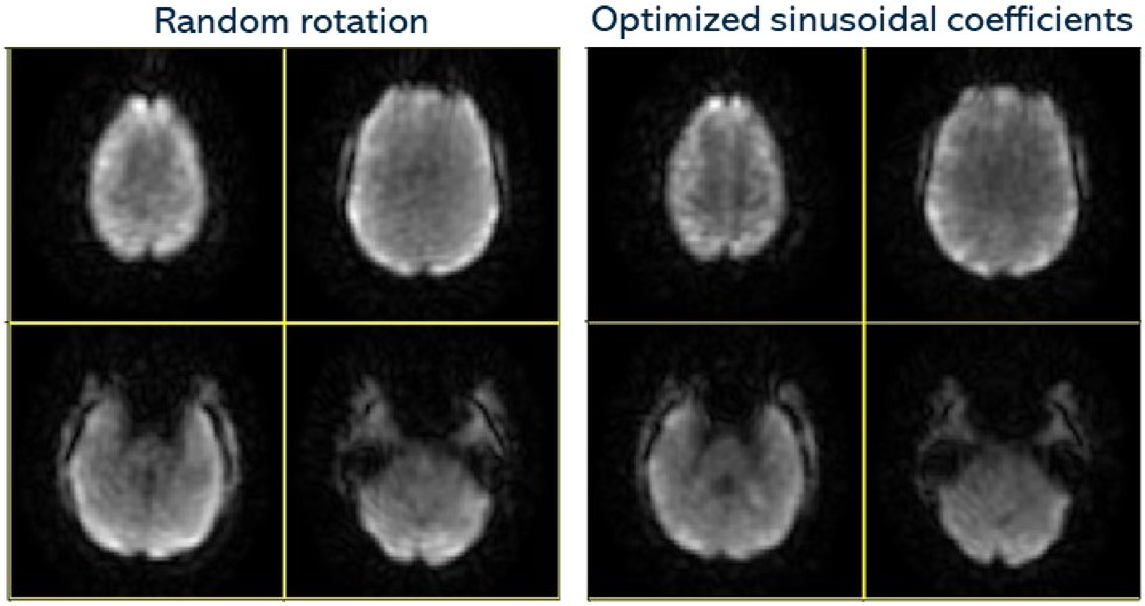

**FIG** 5.4 – Reconstructions for a human brain using the low-resolution protocol (3.75mm isotropic) with random rotations and optimized trajectory. The reconstruction of optimized trajectory lead to better spatial resolution and less image noise as compared to the reconstruction of random rotations.

## 5.5 Discussions

### 5.5.1 Modeling imperfections

In the optimization framework, all of the spokes are modeled and used to optimize the coefficients of the gradient waveforms and trajectories. However, during the actual reconstruction, the last spoke of FID and the first spoke of GRE have different echo time and are overlapped, thus were not used in the reconstruction. This could be considered when optimizing the coefficients to match the actual reconstruction more closely.

Another imperfection is that we used the two main spokes, i.e., echo-in and echo-out spokes, to approximate the acquired signals and construct the system matrices. This works because the center-frequency signal has much larger magnitude than the signals around the edge of the k-space. However, other spokes could be considered at a much higher computational cost.

### 5.5.2 Computational cost

The efficient computation of Jacobian was developed in [50]. In this paper, we aimed to develop an efficient computation for the looping-star Jacobian with two system matrices. Even with the efficient approximation, it still takes weeks to optimize the coefficients using NVIDIA A40 GPU. Further steps, such as more efficient representation of the gradient waveforms, using better initialization, could potentially reduce the computational cost.

## 5.6 Future work

We demonstrated application of the proposed methods to static phantom and in-vivo data. We will test the proposed methods in fMRI by doing finger-tapping and visual fMRI tasks.

# CHAPTER 6

# Preliminary Explorations

In addition to the works discussed in previous chapters, we investigated other reconstruction methods and RF design to further improve the image qualities of the looping-star sequences. Specifically, we explored joint reconstruction approach that simultaneously estimate multiple echoes and relaxation rates to improve the tSNR and reduce noise artifacts. Additionally, we delved into the optimization of RF pulse designs to achieve better magnetization and more uniform signal excitation across the imaging volume. By optimizing the RF pulse flip angle and shape in the looping-star sequence, we aimed to maximize the total magnetization and produce more uniform excitation profiles. Through these investigations, we hope to establish a more robust framework for looping-star MRI that enhances the image qualities and SNR.

## 6.1 Joint reconstruction of T2*-weighted images and quantitative relaxation maps

### 6.1.1 Introduction

Functional magnetic resonance imaging (fMRI) is crucial for the noninvasive imaging of human brain activity, yet the intrusive acoustic noise of MRI poses challenges. This noise can induce discomfort andanxiety, especially in children or dementia patients, and can also confound sensory stimuli, affecting the BOLD response based on its loudness and duration. Looping-Star, a silent MRI pulse sequence, is beneficial for pediatric MRI and auditory fMRI tasks but is hampered by sparse radial sampling and low SNR, restricting its spatial and temporal resolution. We introduce a multi-echo signal collection method in the fMRI protocol to enhance sampling efficiency and SNR. We present a novel joint optimization approach for multi-echo image reconstruction and quantitative map estimation,

---

The work in this chapter is based on author's work [61] and other unpublished preliminary results.

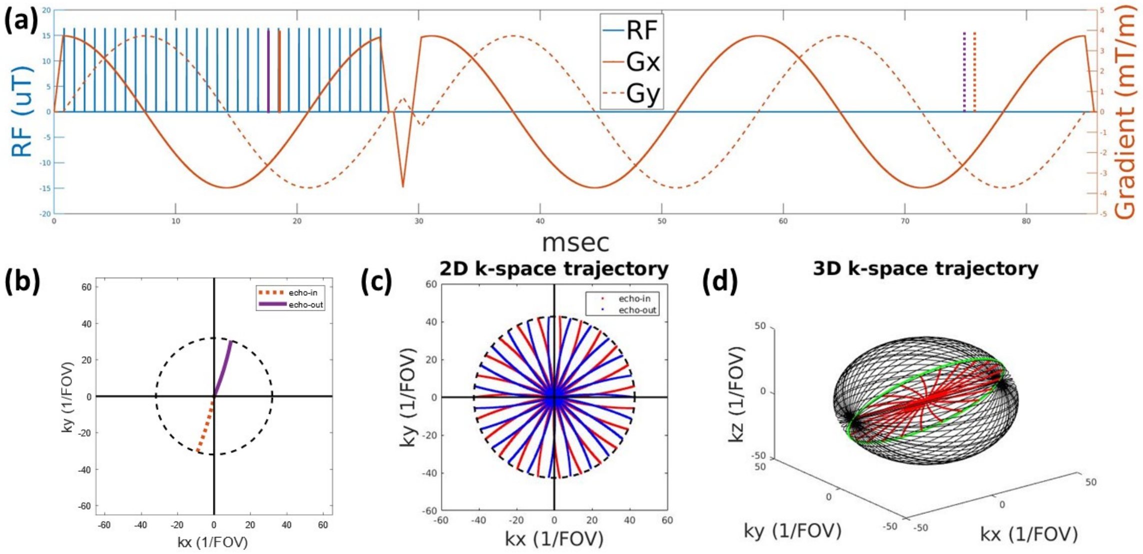

**FIG** 6.1 – (a) A pulse sequence for a 2D plane of the 3D acquisition with one excitation/FID module and two GRE/data acquisition module (ramp-up & down gradient is required by TOPPE), the max slew rate for all modules (including ramps) is 5 mT/m/ms; (b) Illustration of overlapping echoes in GRE module: the echo-out signal from purple RF pulse overlaps the echo-in signal from orange RF pulse in time; (c) 2D GRE k-space trajectory: odd number of spokes are used to generate more evenly distributed spokes; (d) 3D k-space trajectory using 3D generalized golden-angle.

subsequently divided into two sub-problems, that are solved by alternating minimization. After all frames are reconstructed, we use UNFOLD to double the temporal resolution and reduce undersampling artifacts.

### 6.1.2 Methods

#### 6.1.2.1 Pulse sequence

We optimized some parameters to improve the robustness and performance of the pulse sequence. We used a 3D generalized golden-angle-based rotation [28], reduced the number of RF pulses to 23 with increased sampling time, and increased the volume TR to 3.2 sec to reduce the undersampling artifact. Lastly, we collect 2 GRE echoes (as shown in Fig. 6.1)with TE = 30 and 56.9 msec respectively to improve the SNR. The sampling pattern alternates every volume TR to enable UNFOLD [41] filtering after reconstruction.

#### 6.1.2.2 Problem formulation

In Looping-Star MRI, gradient echoes are overlapped in the time domain due to multiple RF pulses. Previous looping-star methods for fMRI typically reconstruct T2*-weighted images from a single set of GRE echoes. In contrast, in this work we use two sets of GRE echoes and then jointly reconstruct the first echo image and the exponential rate map from the k-space data using the following optimization formulation:

$$(\hat{\boldsymbol{\rho}}, \hat{\boldsymbol{z}}) = \underset{\boldsymbol{\rho},\boldsymbol{z}\in\mathbb{C}^N}{\arg\min} \left\| \begin{pmatrix} \boldsymbol{s}_f \\ \boldsymbol{s}_g \end{pmatrix} - \begin{pmatrix} \boldsymbol{A}_f & 0 \\ 0 & \boldsymbol{A}_g \end{pmatrix} \begin{pmatrix} \boldsymbol{\rho} \\ \boldsymbol{\rho}\cdot\boldsymbol{z} \end{pmatrix} \right\|_2^2 + \beta_1 R_1(\boldsymbol{\rho}) + \beta_2 R_2(\boldsymbol{z}), \tag{6.1}$$

where $\boldsymbol{s}_f$ and $\boldsymbol{s}_g$ are signals from FID and GRE respectively, $\boldsymbol{A}_f$ and $\boldsymbol{A}_g$ are systems matrix for FID and GRE that can be computed by (3.5), $\boldsymbol{\rho}$ is the density map, $\boldsymbol{z}(\vec{r}) = e^{-T_{\mathrm{E}}*(\frac{1}{T_2^*(\vec{r})}+\omega(\vec{r}))}$ is the complex decay term due to $T_2^*$ and field inhomogeneity, $R_1(\cdot)$ is regularizer for proton density map, usually a quadratic function in practice, and $R_2(\cdot)$ is regularizer for the rate map.

This optimization problem (6.1) is biconvex and can be solved by alternatively updating $\boldsymbol{\rho}$ and $\boldsymbol{z}$ by fixing one of them and solving the corresponding convex optimization problem [62]. We formulate the sub-problems as follows:

$$\hat{\boldsymbol{\rho}} = \underset{\boldsymbol{\rho}}{\arg\min} \left\| \begin{pmatrix} \boldsymbol{s}_f \\ \boldsymbol{s}_g \end{pmatrix} - \begin{pmatrix} \boldsymbol{A}_f & 0 \\ 0 & \boldsymbol{A}_g \end{pmatrix} \begin{pmatrix} \boldsymbol{I} \\ \boldsymbol{Z} \end{pmatrix} \boldsymbol{\rho} \right\|_2^2 + \beta_1 R_1(\boldsymbol{\rho}), \tag{6.2}$$

and

$$\hat{\boldsymbol{z}} = \underset{\boldsymbol{z}}{\arg\min} \|\boldsymbol{s}_g - \boldsymbol{A}_g \boldsymbol{P} \boldsymbol{z}\|_2^2 + \beta_2 R_2(\boldsymbol{z}), \tag{6.3}$$

where $\boldsymbol{Z} = \mathrm{Diag}\{\boldsymbol{z}\}$ and $\boldsymbol{P} = \mathrm{Diag}\{\boldsymbol{\rho}\}$.

#### 6.1.2.3 Reconstruction

We used CG-SENSE and spatial 3D quadratic roughness regularizers for both $\boldsymbol{\rho}$ and $\boldsymbol{z}$ update. We used 20 outer iterations to alternate between updates and in each of these iterations, we applied 30 CG iterations for the respective updates. The regularization parameters were tuned separately to balance the artifact and effective spatial resolution. Then we used UNFOLD to remove the undersampling artifact from the alternating sampling pattern.

#### 6.1.2.4 Experiments

We compared our proposed joint reconstruction with separate reconstruction of each echo. The pulse sequences were programmed via TOPPE and implemented on a GE UHP 3.0T scanner with a Nova 32RX head coil.

### 6.1.3 Results

Figure 6.2 presents the reconstructed echo images from both separate and joint reconstructions. Echo 1 images resulting from joint reconstruction appear smoother and exhibit fewer streaking artifacts than those from separate reconstruction, likely due to using doubled data during the process. Echo 2 images from 2 methods both suffer from undersampling artifacts and also signal loss. Figure 6.6 displays the tSNR maps derived from the first echo images. Prior to the application of UNFOLD, these maps remain noisy, due to the alternating sampling pattern. As such, the merits of joint reconstruction are not immediately apparent. However, after UNFOLD, tSNR from the joint reconstruction clearly surpasses that of separate reconstruction, particularly near the brain's periphery. By using joint reconstruction, the mean tSNR of a centered elliptical ROI increased from 12.7 to 13.9 before UNFOLD, and 18.0 to 18.5 after UNFOLD. Figure 6.4 illustrates the T2* map estimation and its corresponding tSNR after UNFOLD. The joint estimation approach delivers a superior $T_2^*$ tSNR within the brain relative to separate reconstruction. The mean tSNR of a centered elliptical ROI increased from 16.1 to 18.4.

### 6.1.4 Conclusion

The proposed approach demonstrates enhancements in the reconstructed echo images and the estimated T2* maps, evident both before and after applying UNFOLD. Future research may benefit from investigating additional regularization techniques to address the sub-problems more effectively. These could include edge-preserving regularizers and distinct regularizers for the real and imaginary components of the z map.

## 6.2 Optimization of RF excitation for Silent ZTE MRI

The original looping-star used a constant flip angle scheme below the Ernst angle, i.e., $1^\circ$, to avoid transient $T_1$ effect and keep the length of RF pulse short [16]. However, the flip

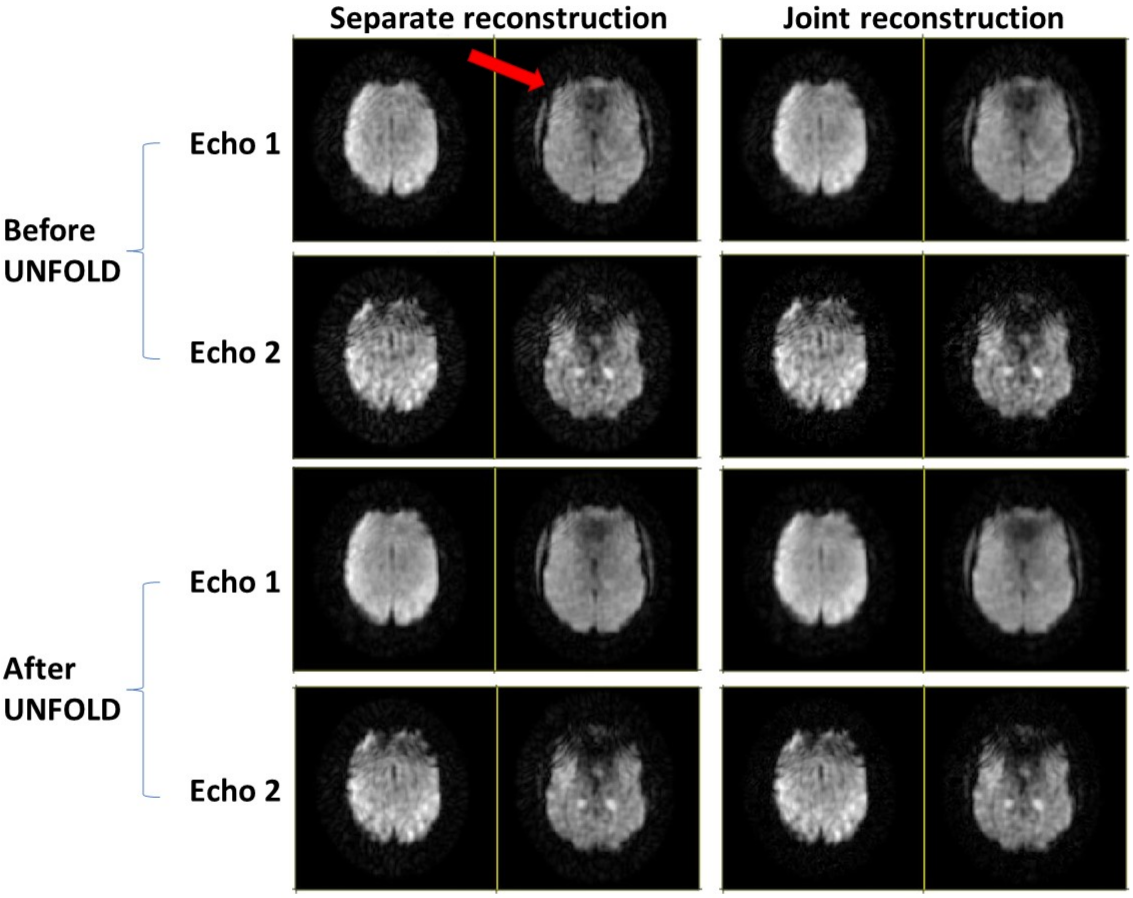

**FIG** 6.2 – The reconstructed echo images from both separate and joint reconstructions. Before UNFOLD, echo 1 images resulting from joint reconstruction appear smoother and exhibit fewer streaking artifacts (red arrow) than those from separate reconstruction, likely due to the utilization of double the data during the process. Echo 2 images from 2 methods both suffer from undersampling artifact and also signal loss. After UNFOLD, the joint reconstruction shows reduced image noise and artifact relative to separate reconstruction.

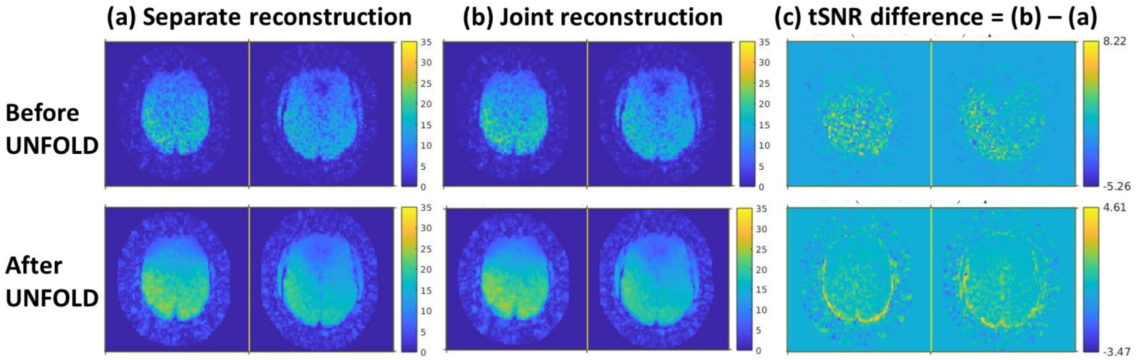

**FIG** 6.3 – The tSNR maps derived from the first echo images. Prior to the application of UNFOLD, these maps remain noisy, attributable to undersampling artifacts from the alternating sampling pattern. As such, the merits of joint reconstruction are not immediately apparent. However, after UNFOLD, tSNR from the joint reconstruction clearly surpasses that of separate reconstruction, particularly near the brain's periphery. By using joint reconstruction, the mean tSNR of an centered elliptical ROI increased from 12.7 to 13.9 before UNFOLD, and 18.0 to 18.5 after UNFOLD.

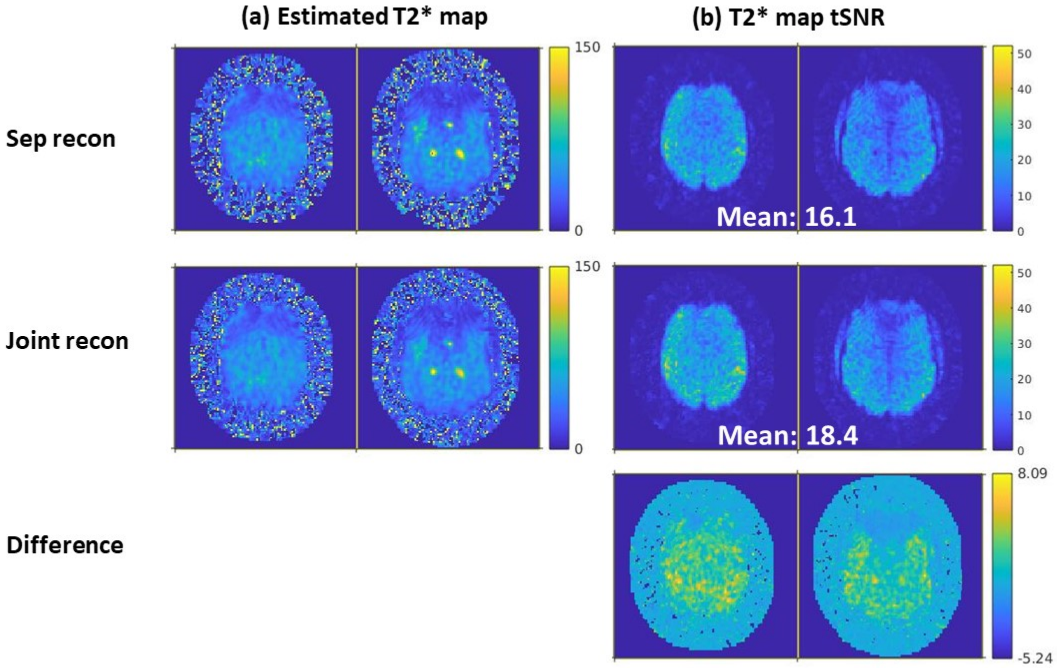

**FIG** 6.4 – The T2* map estimation after UNFOLD and its corresponding tSNR. (a): The T2* map from joint reconstruction shows slightly more smooth T2* estimation. (b) The joint estimation approach delivers a superior T2* tSNR within the brain relative to separate reconstruction. The mean tSNR of a centered elliptical ROI increased from 16.1 to 18.4.

angle can be increased to maximize SNR if the dynamic equilibrium of the longitudinal magnetization could be modeled to create a uniform transverse magnetization. We adapt the Ernst angle derivation to looping-star sequence and compute an optimal constant flip angle. Furthermore, we propose a variable flip angle scheme that further improved the signal amplitude and uniformity over time.

Assume the longitudinal magnetization is in steady-state between blocks, and the flip angle of the $i$th RF pulse is $\alpha_i$, then according to the $T1$ decay

$$M_z^{i+1} = M_0(1 - E_1) + E_1 \cos(\alpha_i)\, M_z^i, \tag{6.4}$$

and

$$M_z^1 = M_0(1 - E_2) + E_2 \cos(\alpha_n)\, M_z^n, \tag{6.5}$$

where $E_1 = e^{-\frac{t_{\mathrm{spk}}}{T1}}$ is the $T1$ decay between the RF pulses, and $E_2 = e^{-\frac{T_{\mathrm{R}}-(n-1)t_{\mathrm{spk}}}{T1}}$ is the $T1$ decay effect between the end of the last RF pulse of current segment and the first RF pulse from next segment.

Combining (6.4) and (6.5) yields

$$M_z^1 = M_0 \frac{(1 - E_2) + E_2(1 - E_1)\sum_{k=1}^{n-1}\prod_{j=0}^{k-1} E_1 \cos(\alpha_{n-j})}{1 - E_{T_{\mathrm{R}}} \prod_{k=1}^{n} \cos(\alpha_k)}, \tag{6.6}$$

where $E_{T_{\mathrm{R}}} = e^{-\frac{T_{\mathrm{R}}}{T1}}$ is the $T1$ decay between segments.

The corresponding transverse plane can be computed by small-tip-angle approximation then.

### 6.2.1 Constant flip angles

In the simplest case that the flip angle is constant over spokes, flip angle can be optimized by maximizing transverse plane signal

$$\hat{\alpha} = \arg\max \alpha M_z^1 \sin(\alpha) = \arg\max_{\alpha} M_0 \frac{(1 - E_2) + E_2(1 - E_1)\frac{1-(E_1\cos(\alpha))^{n-1}}{1-E\cos(\alpha)}}{1 - E_{T_{\mathrm{R}}}(\cos(\alpha))^n} \sin(\alpha)\,. \tag{6.7}$$

This optimization problem can be solved by setting the gradient of (6.7) to zero. It is equivalent to find zeros of a polynomial of order $n$, which can be easily solved by computers.

#### 6.2.1.1 Variable flip angles

When the flip angles are allowed to be varying from spoke to spoke, a series of flip angles $\boldsymbol{\alpha} = \{\alpha_1, \dots, \alpha_n\}$ can be optimized by maximizing either the sum or the minimal transverse plane signals

$$\hat{\boldsymbol{\alpha}} = \arg\max_{\boldsymbol{\alpha}} \sum_{k=1}^{n} M_z^k \sin(\alpha_k) = \arg\max_{\boldsymbol{\alpha}} M_0 \sum_{k=1}^{n} f^k(M_z^1) \sin(\alpha_k), \tag{6.8}$$

where $f(x) = M_0(1 - E) + E\cos(\alpha_i) \cdot x$ is a linear operator from (6.4).

It is hard to explicitly express the gradient of the cost function. This is a differentiable function of the flip angles so it can be optimized numerically using gradient-based algorithms.

#### 6.2.1.2 Linear flip angles

The optimized flip angle by solving (6.8) numerically appears to be nearly linearly increasing, which motivates the following simplified linear version. Assume the cosine values of the flip angles are linearly increasing

$$\cos(\alpha_{i+1}) = \gamma \cos(\alpha_i), \tag{6.9}$$

where $\gamma$ is the parameter controlling the linearity of the flip angles.

Substituting (6.9) into (6.6) gives

$$M_z^1 = \frac{(1 - E_2) + \frac{E_2}{E_1}(1 - E_1) \sum_{k=1}^{n-1} (E_1 \cos(\alpha_1))^k \gamma^{kn - k(k+1)/2}}{1 - E_{T_\mathrm{R}} (\cos(\alpha_1))^n \gamma^{n(n-1)/2}}. \tag{6.10}$$

The corresponding optimization problem in terms of flip angle and linear coefficient $\gamma$ is

$$(\hat{\alpha}_1, \hat{\gamma}) = \arg\max_{\alpha_1, \gamma} \sum_{k=1}^{n} M_z^k \sin(\alpha_k) = \arg\max_{\alpha_1, \gamma} M_0 \sum_{k=1}^{n} f^k(M_z^1) \sin(\alpha_k)\,. \tag{6.11}$$

Solving this problem is much easier since it does not involve repeated multiplication and it generates an excitation profile similar to the previous VFA scheme and maintains good signal amplitude and uniformity.

The current constant flip angle series shows an acceptable longitudinal magnitude and have a decent reconstruction, and the preliminary result using sophisticated design of the flip angle doesn't show great improvement over the constant flip angles in our current

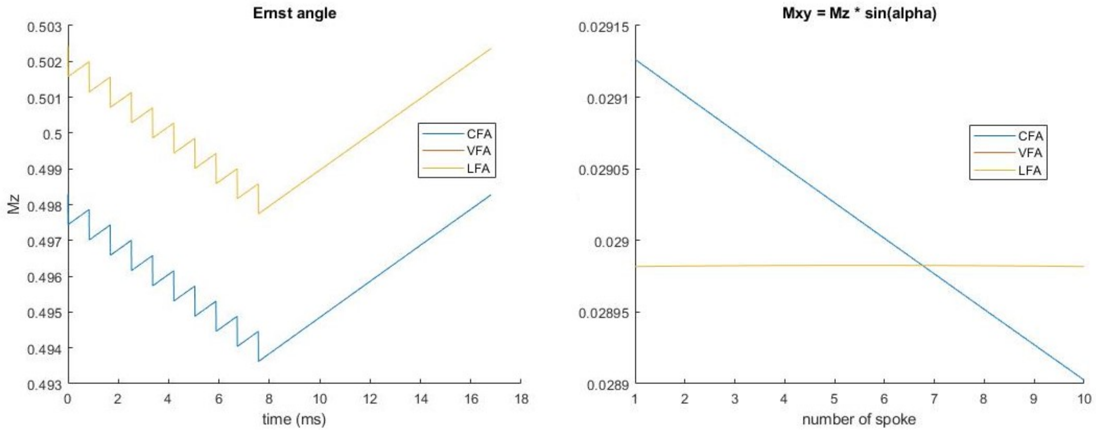

**FIG** 6.5 – The resulting flip angles and corresponding magnetizations. VFA and LFA (overlapped) shows more uniform transverse magnetization than the LFA strategy.

implementation. Therefore, there might not be enough motivation of further developing this flip angles.

### 6.2.2 Shaped RF pulse

Usually many rectangular RF pulses are used to excite the whole field of view (FOV). For low flip angle used in by Dionisio [17], RF pulses is very short and thus the bandwidth is high, so the sinc-shaped shading in spatial domain might not be obvious.

To improve the signal amplitude and uniformity, we use a optimized variable flip angle scheme that is possibly 3 times longer than the original RF pulses. It is then necessary to consider the excitation profile .

The sinc-shaped excitation profile along the readout direction is [24]:

$$P(\vec{r}) = \alpha\,\mathrm{sinc}(\gamma\,\tau\,\vec{G}\cdot\vec{r}), \tag{6.12}$$

where $\alpha = \gamma \boldsymbol{B}_1 \tau$ is the nominal flip angle, $\boldsymbol{B}_1$ is the RF excitation amplitude, $\vec{G}$ is the spoke gradient vector, and $\vec{r}$ is the position vector.

A shaped RF pulse can be designed to increase the uniformity of the excitation profile while minimizing increases in pulse duration. A shaped RF pulse $\boldsymbol{b}$ can be given by solving the following magnitude least square (MLS) problem

$$\hat{\boldsymbol{b}} = \operatorname*{arg\,min}_{\boldsymbol{b}\in\mathcal{B}} f(\boldsymbol{b}), \qquad f(\boldsymbol{b}) \triangleq \frac{1}{2}\left\| |\boldsymbol{A}\boldsymbol{b}| - \boldsymbol{d} \right\|_{\boldsymbol{W}}^{2}, \tag{6.13}$$

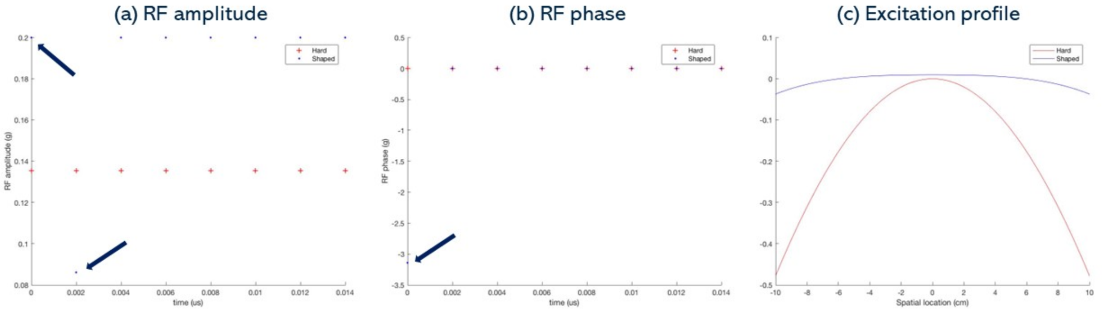

**FIG** 6.6 – The $12\mu$s hard RF pulse and optimized shaped RF pulse (main difference indicated by arrows). (a) RF amplitude; (b) RF phase; (c) resulted excitation profile. Using shaped RF pulse significantly flattened the excitation profile, and maximum absolute flip angle error is reduced from $0.48°$ to $0.03°$

where $\mathcal{B}$ is set of RF pulses that satisfy the peak amplitude constraint, $\boldsymbol{A}$ is the system matrix from small tip angle approximation, and $\boldsymbol{d}$ is the desired excitation profile, usually a flat line.

We solve this MLS problem by alternatively updating RF pulse $\boldsymbol{b}$ and a new introduced variable $\theta$. For the RF pulse update, we use the proximal optimized gradient method (POGM) [42] to optimize the constrained least square problem.

As the current looping-star protocol has a decent uniform excitation profile due to the very short excitation, we plan to investigate further in some applications that have a non-uniform excitation profile. In such cases, shaped RF pulses can be used to improve the reconstruction and analysis.

## CHAPTER 7

# Conclusions and Future Work

## 7.1 Conclusions

This thesis has presented a comprehensive exploration of advanced image reconstruction techniques, sampling pattern optimization, and RF pulse optimization in the context of silent MRI, particularly focusing on the looping-star sequences. In chapter 3, we found that signal modeling using two-system matrices resulted in reduced signal artifact from overlapping echoes and improved SNR of close to 1.4 relative to reconstruction with a single system matrix. Chapter 4 explores spatial-temporal reconstruction using UNFOLD and LLR models, which leverage temporal data from other frames to reduce the undersampling artifact and improve tSNR. In chapter 5, we optimized the k-space trajectories in looping-star using a learning-based method, leading to improved sampling efficiency and reduced undersampling artifact. In chapter 6, we developed joint reconstruction methods, which estimate multiple echoes simultaneously, played a crucial role in improving the temporal signal-to-noise ratio (tSNR) and reducing noise artifacts. Additionally, the optimization of RF pulse designs facilitated better magnetization and more uniform signal excitation across the imaging volume, maximizing total magnetization and achieving more uniform excitation profiles. Collectively, these innovations in model-based image reconstruction, RF pulse design, and k-space trajectory optimization have led to substantial improvements in image quality.

## 7.2 Future Work

### 7.2.1 Acoustic noise level

We roughly measured the acoustic noise level by placing a phone in the scan room and using a phone app to record the noise, then computing the sound level. For more accurate measurements, we would use an MRI-compatible device to measure the sound level in the scanner bore. For the optimized trajectories in Chapter 5, adding higher-order harmonics would increase the slew rate of the gradient waveforms, thereby raising the acoustic noise level. Although we constrain the slew rate and peak gradient amplitude in the cost function, we will investigate further the relationship between higher-order harmonics and the acoustic noise level, including characterizing the gradient to acoustic noise system frequency response function.

### 7.2.2 Model-based reconstruction

For the model-based reconstruction work in Chapter 3, we introduced a voxel indicator function in the reconstruction process. Initially, we implemented this function using the Michigan Image Reconstruction Toolbox (MIRT) in MATLAB [35]. However, as we sought to improve computational efficiency, especially for large dynamic MRI data, we transitioned to using MIRTorch [63]. MIRTorch leverages GPU acceleration, significantly reducing computation times and enabling the handling of more complex spatial-temporal reconstructions. One challenge we encountered during this transition was that the voxel indicator function was not natively available in MIRTorch. To address this, we approximated the voxel indicator function using a weighted least squares problem, which provided a feasible interim solution (as shown in Fig. 7.1). Future work should focus on implementing the voxel indicator function directly in MIRTorch to exactly match the methods used in our original implementation.

In our in-vivo experiment, we did not collect fully sampled data using a standard Cartesian GRE sequence as a reference due to the prohibitively long scan time of 25 minutes. To address this limitation, various undersampling schemes could be employed to acquire a suitable reference dataset more efficiently. One potential approach is to fully sample the center of k-space, which contains the most critical low-frequency information, while undersampling the edges of k-space, which primarily contain high-frequency information. This hybrid sampling method can reduce scan time while still providing a comprehensive reference dataset for comparison and validation purposes.

### 7.2.3 Spatial-temporal reconstruction using DLLR

We will demonstrate functional analysis of the DLLR method with a suitable non-repearting sampling pattern. Also, the LLR and DLLR methods capture important low-rank properties in a manner that is data-driven for each individual subject, but do not capture potential

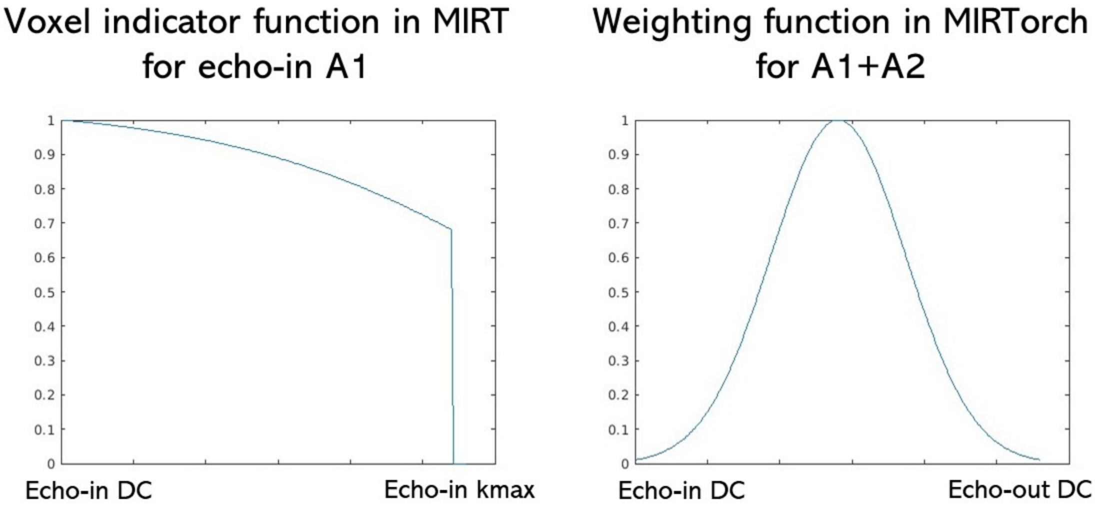

**FIG** 7.1 – Left: 1D voxel indicator function in MIRT. The Fermi filters were applied to each sub-system matrix individually before matrix combination. We chose a 90% cutoff frequency to reduce the mixture of center k-space signals and high-frequency signals coming from the echo-in and echo-out spokes, respectively. Right: 1D weighting function used in MIRTorch. Since a cutoff cannot be applied to the combined system matrix, a Gaussian-shaped weighting is used to suppress the mixture of DC value and high-frequency components.

dimensionality reduction opportunities that could be provided by sparsifying transforms that are refined in a data-driven way using data from multiple subjects. Recent work (for 2D static imaging) has demonstrated that sparsity-based reconstruction methods with as few as about 100 learnable parameters can perform nearly as well as deep networks when trained properly [45]. A future direction is to extend the DLLR approach to a DLLR + sparse (DLLR+S) regularizer using combinations of wavelet transforms (in time and space) and temporal Fourier transforms.

### 7.2.4 Joint reconstruction of multi-echo images

In the joint reconstruction work (Chapter 6), $z$ represents the complex rate map within a unit circle in the complex plane. This constraint can be added to the cost function to ensure that the T2* value remains positive. Another direction is to use different regularization techniques for the field map and the decay map, given their distinct properties. For example, it is commonly assumed that the field map is smooth, allowing the application of quadratic finite difference regularization to it.

### 7.2.5 Trajectories optimization

In optimizing the k-space trajectories (Chapter 5), we focus on optimizing both the amplitude and phase of the proposed parameterization. Alternatively, we could optimize only the amplitude while adding cosine waveforms. These two methods are equivalent in terms of parameterization; however, the derivative of the latter approach is easier to compute, potentially accelerating the optimization process.

### 7.2.6 Deep learning related methods

Recently, deep learning has been widely apply in the field of MRI reconstruction, achieving better results as compared to the tradition model-based methods. ResoNet [64] was proposed to use the noise-trained physics-informed networks to correct the off-resonace in MRI. The data consistency term is included in the network training process to provide the physic information such as k-space trajectories, field map and sensitivity maps. Designing virtual training data for the looping star k-space trajectories using similar approach might be beneficial to train a neural network for the reconstruction. The complex looping trajectories make the signal model complicated and thus accounting all trajectories when solving the inverse problems is not feasible. By using a deep learning based methods, we might be able to leverage the previous data to correct the overlapping echoes without modeling all the RF pulses. Deep learning based reconstruction approach could be one of the potential future directions to further remove overlapping echoes and reduce image noise and artifact.

# BIBLIOGRAPHY

[1] M. Quirk, A. Letendre, R. Ciottone, and J. Lingley. “Anxiety in patients undergoing MR imaging”. In: *Radiology* 170.2 (1989), pp. 463–466 (cit. on pp. 1, 12, 31).

[2] Z. Cho, S. Chung, D. Lim, and E. Wong. “Effects of the acoustic noise of the gradient systems on fMRI: a study on auditory, motor, and visual cortices”. In: *Magnetic resonance in medicine* 39.2 (1998), pp. 331–335 (cit. on pp. 1, 12, 31).

[3] P. Bandettini, A. Jesmanowicz, J. Van Kylen, R. Birn, and J. Hyde. “Functional MRI of brain activation induced by scanner acoustic noise”. In: *Magnetic resonance in medicine* 39.3 (1998), pp. 410–416 (cit. on pp. 1, 12, 31).

[4] N. Yakunina, E. Kang, T. Kim, J. Min, S. Kim, and E. Nam. “Effects of scanner acoustic noise on intrinsic brain activity during auditory stimulation”. In: *Neuroradiology* 57 (2015), pp. 1063–1073 (cit. on pp. 1, 13, 31).

[5] D. Tomasi, E. Caparelli, L. Chang, and T. Ernst. “fMRI-acoustic noise alters brain activation during working memory tasks”. In: *Neuroimage* 27.2 (2005), pp. 377–386 (cit. on pp. 1, 13, 31).

[6] T. Talavage, W. Edmister, P. Ledden, and R. Weisskoff. “Quantitative assessment of auditory cortex responses induced by imager acoustic noise”. In: *Human brain mapping* 7.2 (1999), pp. 79–88 (cit. on pp. 1, 13, 31).

[7] J. Peelle. “Methodological challenges and solutions in auditory functional magnetic resonance imaging”. In: *Frontiers in neuroscience* 8 (2014), p. 253 (cit. on pp. 1, 13, 31).

[8] A. Moelker and P. Pattynama. “Acoustic noise concerns in functional magnetic resonance imaging”. In: *Human brain mapping* 20.3 (2003), pp. 123–141 (cit. on pp. 1, 13, 31).

[9] J. Peelle. “Listening effort: How the cognitive consequences of acoustic challenge are reflected in brain and behavior”. In: *Ear and hearing* 39.2 (2018), p. 204 (cit. on pp. 1, 13, 31).

[10] M. McJury. “Acoustic noise and magnetic resonance imaging: a narrative/descriptive review”. In: *Journal of Magnetic Resonance Imaging* 55.2 (2022), pp. 337–346 (cit. on pp. 1, 13, 31).

[11] W. Edelstein, T. Kidane, V. Taracila, T. Baig, T. Eagan, Y. Cheng, R. Brown, and J. Mallick. “Active-passive gradient shielding for MRI acoustic noise reduction”. In: *Magnetic Resonance in Medicine* 53.5 (2005), pp. 1013–1017 (cit. on pp. 1, 13, 31).

[12] F. Hennel, F. Girard, and T. Loenneker. ““Silent” MRI with soft gradient pulses”. In: *Magnetic Resonance in Medicine* 42.1 (1999), pp. 6–10 (cit. on pp. 1, 13, 31).

[13] D. P. Madio and I. J. Lowe. “Ultra-fast imaging using low flip angles and FIDs”. In: *Magnetic resonance in medicine* 34.4 (1995), pp. 525–529 (cit. on p. 1).

[14] M. Weiger, K. Pruessmann, and F. Hennel. “MRI with zero echo time: hard versus sweep pulse excitation”. In: *Magnetic resonance in medicine* 66.2 (2011), pp. 379–389 (cit. on pp. 1, 13, 31).

[15] D. M. Grodzki, P. M. Jakob, and B. Heismann. “Ultrashort echo time imaging using pointwise encoding time reduction with radial acquisition (PETRA)”. In: *Magnetic resonance in medicine* 67.2 (2012), pp. 510–518 (cit. on p. 1).

[16] F. Wiesinger, A. Menini, and A. Solana. “Looping star”. In: *Magnetic resonance in medicine* 81.1 (2019), pp. 57–68 (cit. on pp. 1, 2, 13, 24, 31, 61).

[17] B. Dionisio-Parra, F. Wiesinger, P. Sämann, M. Czisch, and A. Solana. “Looping star fMRI in cognitive tasks and resting state”. In: *Journal of Magnetic Resonance Imaging* 52.3 (2020), pp. 739–751 (cit. on pp. 1, 2, 13, 19, 24, 31, 66).

[18] C. Matsuo-Hagiyama, Y. Watanabe, H. Tanaka, H. Takahashi, A. Arisawa, E. Yoshioka, S. Nabatame, S. Nakano, and N. Tomiyama. “Comparison of silent and conventional MR imaging for the evaluation of myelination in children”. In: *Magnetic Resonance in Medical Sciences* 16.3 (2017), p. 209 (cit. on pp. 2, 13, 32).

[19] M. Shrestha, H. Lee, U. Nöth, and R. Deichmann. “A novel sequence to improve auditory functional MRI with variable silent delays”. In: *Magnetic Resonance in Medicine* 85.2 (2021), pp. 883–896 (cit. on pp. 2, 13, 32).

[20] N. Damestani, D. Lythgoe, A. Solana, B. Fernandez, S. Williams, F. Zelaya, and F. Wiesinger. “Coherence-resolved Looping Star – improvements for silent multi-gradient echo structural and functional neuroimaging”. In: Proceedings of the 30th Annual Meeting of the ISMRM. Online, 2021, p. 2677 (cit. on pp. 2, 13, 24, 35).

[21] J. Fessler. “Model-based image reconstruction for MRI”. In: *IEEE signal processing magazine* 27.4 (2010), pp. 81–89 (cit. on pp. 2, 14, 16, 17).

[22] H. Xiang, J. A. Fessler, and D. C. Noll. “Model-based reconstruction for looping-star MRI”. In: *Magnetic Resonance in Medicine* 91.5 (2024), pp. 2104–2113. DOI: `https://doi.org/10.1002/mrm.29927` (cit. on pp. 3, 12, 34, 47).

[23] E. Ljungberg, N. L. Damestani, T. C. Wood, D. J. Lythgoe, F. Zelaya, S. C. Williams, A. B. Solana, G. J. Barker, and F. Wiesinger. “Silent zero TE MR neuroimaging: Current state-of-the-art and future directions”. In: *Progress in Nuclear Magnetic Resonance Spectroscopy* 123 (2021), pp. 73–93. ISSN: 0079-6565. DOI: `https://doi.org/10.1016/j.pnmrs.2021.03.002` (cit. on pp. 8–10).

[24] D. M. Grodzki, P. M. Jakob, and B. Heismann. “Correcting slice selectivity in hard pulse sequences”. In: *Journal of Magnetic Resonance* 214 (2012), pp. 61–67 (cit. on pp. 8, 66).

[25] D. O. Kuethe, A. Caprihan, I. J. Lowe, D. P. Madio, and H. Gach. “Transforming NMR Data Despite Missing Points”. In: *Journal of Magnetic Resonance* 139.1 (1999), pp. 18–25. ISSN: 1090-7807. DOI: `https://doi.org/10.1006/jmre.1999.1767` (cit. on p. 8).

[26] A. Haase. “Snapshot FLASH MRI. Applications to T1, T2, and chemical-shift imaging”. In: *Magnetic resonance in medicine* 13.1 (1990), pp. 77–89 (cit. on p. 11).

[27] H. Xiang, J. A. Fessler, and D. C. Noll. “Model-based image reconstruction in looping-star MRI”. In: *Proc. Intl. Soc. Mag. Res. Med.* To appear. 2022 (cit. on pp. 12, 14, 34).

[28] A. Fyrdahl, K. Holst, K. Caidahl, M. Ugander, and A. Sigfridsson. “Generalization of three-dimensional golden-angle radial acquisition to reduce eddy current artifacts in bSSFP CMR imaging”. In: *Magnetic Resonance Materials in Physics, Biology and Medicine* 34 (2021), pp. 109–118 (cit. on pp. 14, 59).

[29] A. Leynes, N. Damestani, D. Lythgoe, A. Solana, B. Fernandez, B. Burns, S. Williams, F. Zelaya, P. Larson, and F. Wiesinger. “Extreme Looping Star: Quiet fMRI at high spatiotemporal resolution”. In: Proceedings of the 30th Annual Meeting of the ISMRM. Online, 2021, p. 0458 (cit. on p. 14).

[30] K. Pruessmann, M. Weiger, P. Börnert, and P. Boesiger. “Advances in sensitivity encoding with arbitrary k-space trajectories”. In: *Magnetic Resonance in Medicine* 46.4 (2001), pp. 638–651 (cit. on pp. 14, 19).

[31] J. Nielsen and D. Noll. “TOPPE: A framework for rapid prototyping of MR pulse sequences”. In: *Magnetic resonance in medicine* 79.6 (2018), pp. 3128–3134 (cit. on pp. 14, 19, 33).

[32] J. Hennig and M. Hodapp. “Burst imaging”. In: *Magnetic Resonance Materials in Physics, Biology and Medicine* 1 (1993), pp. 39–48 (cit. on pp. 14, 33).

[33] R. Chan, E. Ramsay, C. Cunningham, and D. Plewes. “Temporal stability of adaptive 3D radial MRI using multidimensional golden means”. In: *Magnetic Resonance in Medicine* 61.2 (2009), pp. 354–363 (cit. on pp. 15, 34).

[34] B. Sutton, D. Noll, and J. Fessler. “Fast, iterative image reconstruction for MRI in the presence of field inhomogeneities”. In: *IEEE transactions on medical imaging* 22.2 (2003), pp. 178–188 (cit. on p. 17).

[35] J. Fessler. *"Michigan Image Reconstruction Toolbox (MIRT)"*. `https://web.eecs.umich.edu/~fessler/code/index.html` (cit. on pp. 19, 69).

[36] G. Wang, J.-F. Nielsen, J. A. Fessler, and D. C. Noll. “Stochastic optimization of three-dimensional non-Cartesian sampling trajectory”. In: *Magnetic Resonance in Medicine* 90.2 (2023), pp. 417–431 (cit. on pp. 25, 45).

[37] X. Xu, S. Kothapalli, J. Liu, S. Kahali, W. Gan, D. Yablonskiy, and U. Kamilov. “Learning-based motion artifact removal networks for quantitative R2* mapping”. In: *Magnetic resonance in medicine* 88.1 (2022), pp. 106–119 (cit. on p. 25).

[38] H. Xiang, J. A. Fessler, and D. C. Noll. “Spatial-temporal reconstructionusing UNFOLD in looping-star silent fMRI”. In: *Proceedings of the 32th Annual Meeting of the ISMRM.* Vol. 2534. 2023 (cit. on pp. 25, 31).

[39] M. Chiew, S. M. Smith, P. J. Koopmans, N. N. Graedel, T. Blumensath, and K. L. Miller. “k-t FASTER: acceleration of functional MRI data acquisition using low rank constraints”. In: *Magnetic resonance in medicine* 74.2 (2015), pp. 353–364 (cit. on p. 33).

[40] F. Lam, B. Zhao, Y. Liu, Z.-P. Liang, M. Weiner, and N. Schuff. “Accelerated fMRI using low-rank model and sparsity constraints”. In: *Proc. Int. Soc. Magn. Reson. Med. Salt Lake City* (2013), p. 2013 (cit. on p. 33).

[41] B. Madore, G. H. Glover, and N. J. Pelc. “Unaliasing by Fourier-encoding the overlaps using the temporal dimension (UNFOLD), applied to cardiac imaging and fMRI”. In: *Magnetic Resonance in Medicine: An Official Journal of the International Society for Magnetic Resonance in Medicine* 42.5 (1999), pp. 813–828 (cit. on pp. 35, 59).

[42] D. Kim and J. A. Fessler. “Adaptive restart of the optimized gradient method for convex optimization”. In: *Journal of Optimization Theory and Applications* 178.1 (2018), pp. 240–263 (cit. on pp. 37, 67).

[43] C. Y. Lin and J. A. Fessler. “Efficient dynamic parallel MRI reconstruction for the low-rank plus sparse model”. In: *IEEE transactions on computational imaging* 5.1 (2018), pp. 17–26 (cit. on p. 37).

[44] S. Guo, J. A. Fessler, and D. C. Noll. “High-resolution oscillating steady-state fMRI using patch-tensor low-rank reconstruction”. In: *IEEE transactions on medical imaging* 39.12 (2020), pp. 4357–4368 (cit. on p. 37).

[45] H. Gu, B. Yaman, S. Moeller, J. Ellermann, K. Ugurbil, and M. Ak**c** cakaya. “Revisiting 1-wavelet compressed-sensing MRI in the era of deep learning”. In: *Proceedings of the National Academy of Sciences* 119.33 (2022), e2201062119 (cit. on pp. 41, 70).

[46] C. Ahn, J. Kim, and Z. Cho. “High-speed spiral-scan echo planar NMR imaging-I”. In: *IEEE transactions on medical imaging* 5.1 (1986), pp. 2–7 (cit. on p. 45).

[47] P. C. Lauterbur. “Image formation by induced local interactions: examples employing nuclear magnetic resonance”. In: *nature* 242.5394 (1973), pp. 190–191 (cit. on p. 45).

[48] F. A. Breuer, M. Blaimer, M. F. Mueller, N. Seiberlich, R. M. Heidemann, M. A. Griswold, and P. M. Jakob. “Controlled aliasing in volumetric parallel imaging (2D CAIPIRINHA)”. In: *Magnetic Resonance in Medicine: An Official Journal of the International Society for Magnetic Resonance in Medicine* 55.3 (2006), pp. 549–556 (cit. on p. 45).

[49] J. G. Pipe. “Motion correction with PROPELLER MRI: application to head motion and free-breathing cardiac imaging”. In: *Magnetic Resonance in Medicine: An Official Journal of the International Society for Magnetic Resonance in Medicine* 42.5 (1999), pp. 963–969 (cit. on p. 45).

[50] G. Wang and J. A. Fessler. “Efficient Approximation of Jacobian Matrices Involving a Non-Uniform Fast Fourier Transform (NUFFT)”. In: *IEEE Trans. Comput. Imaging* 9 (2023), pp. 43–54. DOI: `10.1109/TCI.2023.3240081` (cit. on pp. 47, 50–52, 57).

[51] R. Remmert. *Theory of complex functions*. Vol. 122. Springer Science & Business Media, 1991 (cit. on pp. 47, 48).

[52] K. Kreutz-Delgado. “The complex gradient operator and the CR-calculus”. In: *arXiv preprint arXiv:0906.4835* (2009) (cit. on p. 48).

[53] A. Hjorungnes and D. Gesbert. “Complex-valued matrix differentiation: Techniques and key results”. In: *IEEE Trans. Sig. Proc.* 55.6 (2007), pp. 2740–2746 (cit. on pp. 48, 49).

[54] Wikipedia contributors. *Numerator layout notation*. [Accessed 2022-11-08]. 2022 (cit. on p. 48).

[55] J. R. Magnus and H. Neudecker. *Matrix differential calculus with applications in statistics and econometrics*. John Wiley & Sons, 2019 (cit. on p. 49).

[56] J. A. Fessler. “Model-based image reconstruction for MRI”. In: *IEEE Sig. Proc. Mag.* 27.4 (July 2010). Invited submission to special issue on medical imaging, 81–9. DOI: `10.1109/MSP.2010.936726` (cit. on pp. 49, 50).

[57] M. R. Hestenes. "Multiplier and Gradient Methods". In: *J. Optim. Theory Appl.* 4.5 (Nov. 1969), pp. 303–320. DOI: `10.1007/BF00927673` (cit. on p. 51).

[58] H. K. Aggarwal, M. P. Mani, and M. Jacob. "MoDL: model-based deep learning architecture for inverse problems". In: *IEEE Trans. Med. Imag.* 38.2 (Feb. 2019), 394–405. DOI: `10.1109/tmi.2018.2865356` (cit. on pp. 51, 52).

[59] S. Ramani and J. A. Fessler. "Parallel MR image reconstruction using augmented Lagrangian methods". In: *IEEE Trans. Med. Imag.* 30.3 (Mar. 2011), 694–706. DOI: `10.1109/TMI.2010.2093536` (cit. on p. 51).

[60] S. H. Chan, X. Wang, and O. A. Elgendy. "Plug-and-play ADMM for image restoration: fixed-point convergence and applications". In: *IEEE Trans. Computational Imaging* 3.1 (Mar. 2017), 84–98. DOI: `10.1109/tci.2016.2629286` (cit. on p. 51).

[61] H. Xiang, I. K. Onder, A. H. Mehta, J. A. Fessler, and D. C. Noll. "Joint optimization of multi-echo reconstruction and quantitative map estimation in Looping Star". In: *Proceedings of the 33th Annual Meeting of the ISMRM.* Vol. 0630. 2024 (cit. on p. 58).

[62] J. Gorski, F. Pfeuffer, and K. Klamroth. "Biconvex sets and optimization with biconvex functions: a survey and extensions". In: *Mathematical methods of operations research* 66.3 (2007), pp. 373–407 (cit. on p. 60).

[63] G. Wang, N. Shah, K. Zhu, D. Noll, and J. Fessler. "MIRTorch: A PyTorch-powered differentiable toolbox for fast image reconstruction and scan protocol optimization". In: *Proceedings of International Society of Magnetic Resonance in Medicine 31st Annual Conference.* 2022 (cit. on p. 69).

[64] A. De Goyeneche, S. Ramachandran, K. Wang, E. Karasan, J. Cheng, S. X. Yu, and M. Lustig. "Resonet: Noise-trained physics-informed MRI off-resonance correction". In: *Thirty-seventh Conference on Neural Information Processing Systems.* 2023 (cit. on p. 71).